



Thermal properties of Pluto's and Charon's surfaces from observations

Emmanuel Lellouch, John Stansberry, Josh Emery, Will Grundy, Dale P. Cruikshank

► To cite this version:

Emmanuel Lellouch, John Stansberry, Josh Emery, Will Grundy, Dale P. Cruikshank. Thermal properties of Pluto's and Charon's surfaces from observations. *Icarus*, 2011, 214 (2), pp.701. <10.1016/j.icarus.2011.05.035>. <hal-00786880>

HAL Id: hal-00786880

<https://hal.science/hal-00786880v1>

Submitted on 11 Feb 2013

HAL is a multi-disciplinary open access archive for the deposit and dissemination of scientific research documents, whether they are published or not. The documents may come from teaching and research institutions in France or abroad, or from public or private research centers.

L'archive ouverte pluridisciplinaire **HAL**, est destinée au dépôt et à la diffusion de documents scientifiques de niveau recherche, publiés ou non, émanant des établissements d'enseignement et de recherche français ou étrangers, des laboratoires publics ou privés.



HAL Authorization

Accepted Manuscript

Thermal properties of Pluto's and Charon's surfaces from *Spitzer* observations

Emmanuel Lellouch, John Stansberry, Josh Emery, Will Grundy, Dale P. Cruikshank

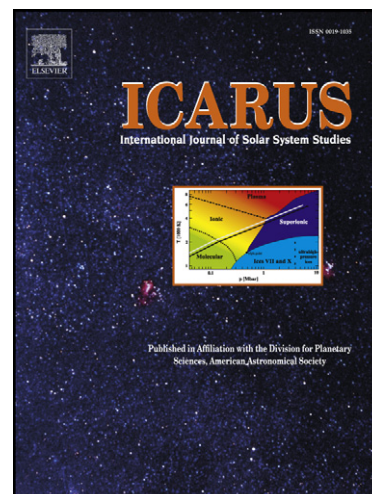
PII: S0019-1035(11)00208-9
DOI: [10.1016/j.icarus.2011.05.035](https://doi.org/10.1016/j.icarus.2011.05.035)
Reference: YICAR 9842

To appear in: *Icarus*

Received Date: 4 February 2011
Revised Date: 11 May 2011
Accepted Date: 25 May 2011

Please cite this article as: Lellouch, E., Stansberry, J., Emery, J., Grundy, W., Cruikshank, D.P., Thermal properties of Pluto's and Charon's surfaces from *Spitzer* observations, *Icarus* (2011), doi: [10.1016/j.icarus.2011.05.035](https://doi.org/10.1016/j.icarus.2011.05.035)

This is a PDF file of an unedited manuscript that has been accepted for publication. As a service to our customers we are providing this early version of the manuscript. The manuscript will undergo copyediting, typesetting, and review of the resulting proof before it is published in its final form. Please note that during the production process errors may be discovered which could affect the content, and all legal disclaimers that apply to the journal pertain.



Thermal properties of Pluto's and Charon's surfaces from *Spitzer* observations

Emmanuel Lellouch

*LESIA, Observatoire de Paris, 5 place Jules Janssen, F-92195 Meudon, France;
emmanuel.lellouch@obspm.fr*

John Stansberry

*Steward Observatory, University of Arizona, 933 North Cherry Avenue, Tucson AZ
85721-0065, USA*

Josh Emery

*Department of Earth and Planetary Sciences, University of Tennessee, 1412 Circle
Drive, Knoxville, TN 37996-1410, USA*

Will Grundy

Lowell Observatory, 1400 W. Mars Hill Rd., Flagstaff AZ 86001, USA

Dale P. Cruikshank

Astrophysics Branch, NASA Ames Research Center, Moffett Field, CA 94035-1000, USA

Abstract

We report on thermal observations of the Pluto–Charon system acquired by the *Spitzer* observatory in August–September 2004. The observations, which consist of (i) photometric measurements (8 visits) with the Multiband Imaging Photometer (MIPS) at 24, 70 and 160 μm and (ii) low-resolution spectra (8 visits) over 20 – 37 μm with the Infrared Spectrometer (IRS), clearly exhibit the thermal lightcurve of Pluto/Charon at a variety of wavelengths. They further indicate a steady decrease of the system brightness temperature with increasing wavelength. Observations are analyzed by means of a

thermophysical model, including the effects of thermal conduction and surface roughness, and using a multi-terrain description of Pluto and Charon surfaces in accordance with visible imaging and lightcurves, and visible and near-infrared spectroscopy. Three units are considered for Pluto, respectively covered by N₂ ice, CH₄ ice, and a tholin/H₂O mix. Essential model parameters are the thermal inertia of Pluto and Charon surfaces and the spectral and bolometric emissivity of the various units. A new and improved value of Pluto's surface thermal inertia, referring to the CH₄ and tholin/H₂O areas, is determined to be $\Gamma_{Pl} = 20\text{--}30 \text{ J m}^{-2} \text{ s}^{-1/2} \text{ K}^{-1}$ (MKS). The high-quality 24- μm lightcurve permits a precise assessment of Charon's thermal emission, indicating a mean surface temperature of $55.4 \pm 2.6 \text{ K}$. Although Charon is on average warmer than Pluto, it is also not in instantaneous equilibrium with solar radiation. Charon's surface thermal inertia is in the range $\Gamma_{Ch} = 10\text{--}150 \text{ MKS}$, though most model solutions point to $\Gamma_{Ch} = 10\text{--}20 \text{ MKS}$. Pluto and Charon thermal inertias appear much lower than values expected for compact ices, probably resulting from high surface porosity and poor surface consolidation. Comparison between Charon's thermal inertia and even lower values estimated for two other H₂O-covered Kuiper-Belt objects suggests that a vertical gradient of conductivity exists in the upper surface of these bodies. Finally, the observations indicate that the spectral emissivity of methane ice is close to unity at 24 μm and decreases with increasing wavelength to ~ 0.6 at 100 μm . Future observations of thermal lightcurves over 70–500 μm by *Herschel* should be very valuable to further constrain the emissivity behaviour of the Pluto terrains.

Key words: Pluto; Pluto, surface; Charon; Infrared observations

1. Introduction

Once a “singularly freakish and unexplained anomaly in the Outer Solar System” (D. Jewitt), Pluto and its system can now be seen as a benchmark for Kuiper Belt studies. By far the best observed member of this family, Pluto is one of the very few trans-neptunian objects (along with Haumea, Lacerda et al. 2008) for which spatial heterogeneity is unambiguously demonstrated. Optical lightcurves and their secular variability (e.g. Buie et al. 1997, 2010a, and references therein), mutual events of the Pluto-Charon system over 1985–1990 (e.g. Buie et al. 1992, Young et al. 1999, 2001), direct HST imaging in several colors (Stern et al. 1997, Buie et al. 2010b), and the monitoring and modelling of Pluto’s visible and infrared spectrum (e.g. Grundy and Fink, 1996, Douté et al. 1999, Grundy and Buie 2001, 2002, Olkin et al. 2007, Protopapa et al. 2008, Merlin et al. 2010) all show that Pluto’s surface is covered by ices of different kinds (N_2 , CO , CH_4 , H_2O /tholins, and perhaps additional compounds such as ethane) with uneven distributions, leading to large albedo variations across the surface. Ultimately, this variegation and the likely seasonal variability (Schaefer et al. 2008) of terrain distribution must be related to transport and condensation/sublimation exchanges between the surface and Pluto’s tenuous N_2 -dominated atmosphere. Albedo contrasts and the diurnal/latitudinal variability of insolation are associated with local temperature contrasts, as demonstrated by the existence of a thermal lightcurve of the Pluto-Charon system, first observed (marginally) by IRAS (Sykes 1999) and then much more clearly by ISO in 1997 (Lellouch et al. 2000). Analysis of the ISO data (especially at 60 and 100 μm) revealed the thermal lightcurve to be approximately but not strictly anti-correlated

with its optical counterpart, a behaviour attributed to thermal inertia effects. Multi-terrain modelling of these data indicated a thermal inertia of $\Gamma = (1.5\text{--}10) \times 10^4 \text{ erg cm}^2 \text{ s}^{1/2} \text{ K}^1$ (i.e. 15–100 in the more conventional MKS $\text{J m}^{-2} \text{ s}^{-1/2} \text{ K}^{-1}$ unit) for Pluto’s surface, the first constraint on thermal conductivity on a Kuiper-Belt object.

Charon’s surface is less well known than Pluto’s. This stems from (i) its ~ 2 times smaller diameter, which puts it at the limit of current technology for direct imaging (ii) its less rich spectrum, overwhelmingly dominated by crystalline H_2O ice, with some amounts of NH_3 , possibly in hydrated form (Cook et al. 2007, Merlin et al. 2010). In the absence of surface volatiles and atmospheric cycles on Charon, its surface seems much more uniform than Pluto’s, with little if any longitudinal structure in HST images (Buie et al. 2010b) and a weak optical lightcurve (peak-to-peak amplitude ~ 0.09 mag, vs ~ 0.26 mag for Pluto, for observations taken in 2002, see Buie et al. 2010a). Thermal properties of Charon remain poorly constrained, given that thermal observations usually do not separate Pluto from Charon. An exception is provided by millimeter interferometric measurements of Pluto/Charon with $\sim 0.5''$ resolution (Gurwell and Butler 2005, Gurwell et al. 2010), indicating a mean 1.4 mm brightness temperature higher for Charon than Pluto ($\sim 49 \text{ K}$ vs $\sim 37 \text{ K}$), which is to be expected given Charon’s lower geometric albedo. Due to its higher temperature, the relative contribution of Charon to the thermal flux in spatially unresolved observations must increase with decreasing wavelength and ultimately dominate over Pluto’s.

With its MIPS (photometry at 24, 70 and $160 \mu\text{m}$) and IRS (low-resolution spectroscopy from 5 to $38 \mu\text{m}$) instruments, the *Spitzer* Space Telescope

(Werner et al. 2004) is well suited to measure the thermal emission from the Pluto-Charon system over a more extended wavelength range. We report here on combined MIPS and IRS observations obtained in August-September 2004, which provide new constraints on the thermal properties of the two bodies. Preliminary assessment and modelling of these data have been reported (Lellouch et al. 2006a, 2006b, Stansberry et al. 2009), but the present analysis, which makes use of recently published quasi-contemporary Pluto and Charon lightcurves and images (Buie et al. 2010a, b), supersedes the earlier results. Observations and data reduction are presented in Section 2. The thermal model is described in Section 3, and inferences on the thermophysical and surface properties of Pluto and Charon are drawn in Sections 4 and 5. Finally, results are discussed in Section 6. Additional MIPS observations were acquired in April 2007, September 2007, and October 2008. Except for a brief glimpse into the April 2007 data at the end of this paper, these measurements will be presented elsewhere.

2. Observations and data reduction

2.1. MIPS observations

We obtained far-IR photometry of Pluto using the Multiband Imaging Photometer for *Spitzer* (MIPS; Rieke et al. 2004) at wavelengths near 24, 70 and 160 μm , spanning the peak of Pluto's thermal emission. The *Spitzer* PSF encompasses the entire Pluto system at all three wavelengths, thus including emission from Pluto and Charon (as well as the negligible contributions of Nix and Hydra). The data were collected in September 2004 under the *Spitzer* program ID 70. They were taken in 8 discrete visits timed to span a full

rotation of Pluto, providing a multi-band thermal light curve. Integration times in the three wavelength channels (which were observed in sequence, 24 – 70 – 160 μm , during each visit) were 506, 330 and 602 seconds. The signal-to-noise ratio (SNR) of the single-visit detections is about 25 in the 24 μm channel and about 15 in the 70 μm channel. The 160 μm data is of significantly lower quality, with a nominal SNR of about 5, and a degraded absolute calibration accuracy (see below).

We reduced the data using the MIPS instrument team data analysis tools (Gordon et al. 2005), producing flux-calibrated images for each band and each visit. Post-processing was performed to subtract away the contribution from background objects in the Galactic plane. The full reduction, calibration, post-processing, photometry, and conversion to monochromatic fluxes have been described elsewhere (e.g. Stansberry et al. 2006, 2007, 2008, 2011). Note that the effective wavelengths for the 24, 70 and 160 micron channels are defined to be 23.68, 71.42 and 156 μm , and that color corrections are modest. Even at 24 μm , where Pluto's spectrum is much redder than the MIPS stellar calibrators, the correction is only $\sim 10\%$, and the uncertainty on this number is even smaller. The MIPS absolute calibration is accurate to 2%, 4% and 6% (see below for more on the 160 μm uncertainty) in those channels, respectively (Gordon et al. 2007, Engelbracht et al. 2007, Stansberry et al. 2007). To allow for the effects of our post-processing, uncertainties in the color correction and the fact that our target moves (the calibration is based on stellar observations), we inflated the calibration uncertainties by 50 %. For the final uncertainty on the fluxes we root-sum-square combined the calibration uncertainty with the photometric measurement uncertainty,

estimated from the sky surrounding the source in the images. One observation (epoch 2004-09-17 23:22, East longitude $L = 36.7^\circ$)¹ was impacted by a bright main-belt asteroid (665 Judith) that appeared very near Pluto. For data from that visit we subtracted a model PSF from the images to remove the signal from the asteroid, and performed photometry on the resulting images.

The 160 μm data were more difficult to process. In images produced by the standard processing techniques, Pluto was barely distinguishable at 160 μm . By applying time-domain filtering to the data (which is a standard part of the 70 μm processing, but not for 160 μm), the SNR of the Pluto detection was greatly enhanced. A complication arose because the calibration of the 160 μm channel relies on the un-filtered processing (Stansberry et al. 2007). We processed observations of faint 160 μm calibration targets (asteroids) using time-domain filtering to try and determine its effect on the absolute calibration. However, there were only a few such targets, and the comparison of their measured fluxes in the standard and time-filtered data products did not indicate a systematic difference, but did show discrepancies at the 10% level for individual observations. As a result, we used an absolute calibration uncertainty of 15%, rather than the nominal value of 6 % stated earlier.

Figure 1 shows all visit images for all three MIPS bands. Table 1 summarizes the epochs, observing circumstances, and the full dataset, i.e. the monochromatic 23.68, 71.42 and 156 μm fluxes and their error bars. The

¹Throughout the paper, we adopt the same orbital conventions as e.g. in Buie et al. (1997) and Lellouch et al. (2000), in which the sub-observer longitude decreases with time and the Northern hemisphere is currently in Summer.

mean heliocentric distance for these observations is 30.847 AU. The MIPS fluxes are shown in Fig. 2, after rescaling to a common (arbitrary) distance to the observer of 30.95 AU. Fig. 2 shows a clear detection of Pluto/Charon thermal lightcurve at $24\ \mu\text{m}$, with maximum flux near $L = 80$, minimum flux near $L = 220$, and a 60 % amplitude (i.e. a maximum/minimum flux ratio of ~ 1.6). The lightcurve is more marginally detected at $70\ \mu\text{m}$, with a ~ 30 % amplitude, and not apparent in the lower-quality $160\ \mu\text{m}$ data.

2.2. IRS observations

Thermal infrared spectra of Pluto/Charon were measured using the Infrared Spectrograph (IRS; Houck et al. 2004) on board *Spitzer* in August–September 2004. IRS measures spectra from 5.2 to $38\ \mu\text{m}$ in four segments with resolving power $R \sim 64$ to 128 . A higher spectral resolution, cross-dispersed mode ($R \sim 600$) is also available, but was not used here. Because thermal emission from the Pluto system is below IRS detection limits at $\lambda < 20\ \mu\text{m}$, spectra were only collected in the longest wavelength module (LL1). The resulting spectra cover the spectral range 19.5 to $38.0\ \mu\text{m}$. The LL1 slit is much wider ($10.5\ \text{arcsec}$) than the blind pointing accuracy of the observatory ($\sim 1\ \text{arcsec}$), so the optional peak-up pointing refinement observations were not used for these spectral measurements. Observations were acquired at 8 different longitudes, evenly distributed across the surface (see Table 2). The observations employed standard nodding, in which data were taken at two positions along the slit, separated by about $50\ \text{arcsec}$. At each position, three 120 sec frames were taken, for a total on-source integration time of 720 sec for each of the 8 longitudes observed.

All raw data returned by IRS are run through a data reduction pipeline.

This pipeline converts the three dimensional raw data files into 2-D image files and performs many of the normal steps associated with infrared spectral data processing, including dark current subtraction, flat field corrections, bad pixel identification, cosmic ray mitigation, as well as several instrument specific steps such as non-linearity corrections and stray light removal. These steps are described in detail in the IRS instrument handbook (<http://ssc.spitzer.caltech.edu/irs/irsinstrumenthandbook/>). The output of the pipeline is the Basic Calibrated Data (BCD), which consist of 2-D spectral images that include both source and background flux. We began our spectral extraction by subtracting the two nod positions for a given observation from each other to remove the background flux. Spectra were extracted by summing the flux at each wavelength within an extraction window, set at about the FWHM of the point-response function (PRF) at that wavelength. Since *Spitzer* is diffraction limited, the PRF is a function of wavelength, so the extraction window increases in width with increasing wavelength. Both absolute and relative spectral calibration parameters are provided by the *Spitzer*/IRS team. However, we used a custom extraction procedure (allowing us to vary several of the extraction parameters, including width), so we also calculated refinements to the nominal calibration parameters by reducing several stellar calibrators (HR 7341, HD 173511, and HR 6688) with the same settings used for Pluto. Point-to-point uncertainties are calculated in the data pipeline from counting statistics and propagated through all stages of data reduction. Additionally, the *Spitzer*/IRS team has determined that the absolute flux calibration of IRS is good to about $\pm 5\%$.

The IRS spectra are presented in Fig. 3 in brightness temperature (T_B)

units for the Pluto-Charon system. For this, individual radii of 1170 and 604 km for Pluto and Charon respectively were assumed (see below). By a fortunate occurrence, each of the 8 IRS visits to Pluto can be associated with one of the 8 MIPS visits, with longitudes coinciding to within $2\text{--}7^\circ$ of longitude. Taking advantage of this, Fig. 3 also includes the MIPS 24, 70 and $160\text{ }\mu\text{m}$ photometric points (colored circles), showing excellent consistency between the $24\text{ }\mu\text{m}$ MIPS photometry and the IRS spectra at similar longitudes. This warrants the possibility to model jointly the MIPS and IRS spectra. The slight difference in heliocentric distance for the IRS (30.836–30.840 AU) and MIPS (30.846–30.849 AU) data can be ignored, as leading to variations of the brightness temperatures at the 0.01 K level only. Fig. 3 also includes photometric points from ISO obtained in 1997 (Lellouch et al. 2000), rescaled in an approximate fashion to the 2004 heliocentric distance (i.e. corrected for $R_h^{-1/2}$).

Mean (rotation-averaged) brightness temperatures of the Pluto-Charon system show a steady decrease with increasing wavelength (λ), with e.g. ~ 52 K at $24\text{ }\mu\text{m}$, ~ 50 K at $37\text{ }\mu\text{m}$ and ~ 46 K at $71\text{ }\mu\text{m}$, and further declining at longer λ s. This behaviour can be produced in three ways: (i) a spatially constant surface temperature T and a low (spectrally constant) surface emissivity ϵ (ii) the mixing of different surface temperatures (iii) a decrease of the spectral emissivity with wavelength. Option (i) is technically possible, but unlikely given the observed albedo variegation on Pluto; additionally it would require $T \sim 57$ K and an improbably low ($\epsilon \sim 0.45$) surface emissivity. Option (ii) is more likely, as at least in a quantitative sense, the superposition of Planck functions does produce a decrease of T_B with λ . However, the

detailed, multi-terrain modelling presented below suggest that a decrease of the spectral emissivity with λ of some of the Pluto areas is also required.

3. Modelling

3.1. Thermophysical model

Modelling of the MIPS and IRS data was performed using a thermophysical, multiple terrain, model of the Pluto-Charon system, similar to that used for the analysis of the ISO data (Lellouch et al. 2000). The thermophysical model includes subsurface conduction as well as surface roughness effects. Thermal inertia effects are described through the standard dimensionless thermal parameter Θ (see Spencer et al. 1989), representing the ratio of the radiation timescale of subsurface heat to the diurnal timescale:

$$\Theta = \frac{\Gamma \sqrt{\omega}}{\epsilon_b \sigma T_{SS}^3} \quad (1)$$

Here Γ is the thermal inertia, ω is the body rotation rate, ϵ_b is the bolometric emissivity of the surface, σ is Stefan-Boltzmann's constant and T_{SS} is the instantaneous equilibrium temperature as the subsolar point, given by $T_{SS} = (\frac{1-A_b}{\epsilon_b} \frac{F}{\sigma R_h^2})^{1/4}$, where A_b is the bolometric albedo, F the solar constant at 1 AU and R_h is the heliocentric distance in AU.

Local temperatures on Pluto and Charon are thus expressed as:

$$T = \frac{T_{SS}}{\eta_{TPM}(\Theta)^{1/4}} \times f(\text{latitude}, \text{local time}, \Theta) \quad (2)$$

where $f(\text{latitude}, \text{local time}, \Theta)$ is a normalized temperature function, depending on the thermal parameter and on insolation (through the local latitude, local time, and subsolar latitude), and calculated following Spencer

et al. (1989). The $\eta_{TPM}(\Theta)$ factor (thermophysical model beaming factor) allows one to include surface roughness effects, as detailed hereafter and in Lellouch et al. (2000). Although the formalism is the same, $\eta_{TPM}(\Theta)$ should not be confused with the $\eta (= \eta_{STM})$ factor introduced in the STM (Standard Thermal Model, Spencer et al. 1989), NEATM (Near-Earth Asteroid Thermal Model, Harris 1998) and hybrid-STM (Stansberry et al. 2008) models: $\eta_{TPM}(\Theta)$ is introduced within the thermophysical model, and includes only the effects of roughness (therefore, $\eta_{TPM}(\Theta) < 1$), while η_{STM} globally and empirically accounts for thermal inertia, pole orientation, and roughness effects (and can be >1). Our model does not explicitly include sublimation or condensation terms, although special conditions (see below) allow us to account for such effects in a simplified way. Once local temperatures are calculated, the local flux at a given wavelength λ is calculated as $\epsilon_\lambda B_\lambda(T)$ where B_λ is the Planck function and ϵ_λ is the spectral emissivity. As our models include several surface units (see below), individual A_b , ϵ_b and ϵ_λ values for each unit are used. Local fluxes are summed (and the result converted into brightness temperatures) for comparison to the data.

3.2. Surface units

Following Grundy and Fink (1996), Lellouch et al. (2000) and Grundy and Buie (2001), we considered three surface units on Pluto, respectively dominated by (i) (unit 1): bright N_2 ice (with small amounts of dissolved CO and CH_4) (ii) (unit 2): pure CH_4 ice, of intermediate albedo and (iii) (unit 3): dark H_2O ice / tholin mix. Grundy and Fink (1996) and Grundy and Buie (2001) proposed several geographical distributions for these units, meant to account for Pluto's visible lightcurve (Buie et al. 1997), general

appearance in mutual event (Buie et al. 1992) and HST (Stern et al. 1997) maps, and the rotational variability of CH_4 , N_2 and CO ice features in the near-infrared. Specifically, we here considered the five distributions of surface units discussed by Grundy and Buie (2001), respectively termed in that paper as 1) “Grundy and Fink” 2) “Lellouch et al.” 3) “Modified Grundy and Fink” 4) “Sliced HST” 5) “Modified HST”. We here adopt this terminology, and the five distributions are labelled hereafter as g_1 , g_2 , g_3 , b_1 and b_3 , respectively. Briefly, distribution g_1 was designed by Grundy and Fink (1996) on the basis of the original Buie et al. (1992) albedo map and the longitudinal behaviour of the methane visible bands in their own observations. It was used as such by Lellouch et al. (2000) and then slightly modified by the same authors in such a manner (distribution g_2) that the relative coverage of the various units agreed better with the proportions inferred from a detailed analysis of 1–2.5 μm spectra (Douté et al. 1999). Further changes to these two distributions were implemented by Grundy and Buie (2001) to improve consistency with the longitudinal variability of the weak methane features and of the N_2 2.15 μm band in their spectra (distribution g_3). Distribution b_1 was designed by the same authors by “slicing” a HST/WFPC2 map obtained in 1994 (an early version of which was presented by Stern et al. 1997) into three visual albedo levels and assigning them to the same compositional units. Finally, distribution b_3 was an alternative map based on these HST data, in which zones at the regional scale are composed of “checker-board” mixtures of different units (as opposed to consisting of a single unit), providing a closer match to the original HST albedo map. The five distributions are shown in Fig. 4. Before proceeding, we note that while this depiction of Pluto’s

surface in terms of three units, geographically segregated according to their volatility, is reasonable and has been traditionally used a number of papers, it is admittedly a simplified description of Pluto’s reality. In particular, since CO is assumed (as expected thermodynamically) to be co-condensed with N₂ in unit 1, the adopted description cannot explain the different longitudinal distributions of N₂ 2.15 μm and CO 1.58 μm ice features, showing notably enhanced CO absorption near longitudes $L = 180$ (Grundy and Buie 2001), in a region apparently associated with the brightest point in the HST map (Buie et al. 2010b).

For a given geographical distribution, we first determined the equivalent geometric albedos of each unit that allowed best fitting of Pluto’s optical lightcurve. For the latter, we used the V lightcurve measured by HST in 2002–2003 (Buie et al., 2010a), hence close in time to the *Spitzer* observations, converted to geometric albedo assuming a 1170 km radius and Lambertian scattering behavior, and using the proper geometry (sub-observer latitude $\sim +31^\circ$). Pluto’s radius remains uncertain, and the above value is a compromise between results from mutual events, stellar occultations, and near-infrared spectroscopy (see Lellouch et al. 2009). The inferred geometric albedos are given in Table 3 for each of the five distributions, and the fits of the Buie et al. (2010a) Pluto lightcurve are shown in Fig. 5. Distributions g_1 – g_3 allow a generally good match of the observed lightcurve, especially over $L = 0$ –240 East longitudes, while the two HST-derived distributions provide significantly worse fits, notably over $L = 50$ –120 (corresponding to a large, dark, region on Pluto’s surface). Moreover, in the best fit solution for the “Sliced HST” distribution, the inferred albedo for the CH₄ (0.80) is larger

than for N_2 , inconsistent with the concept that the brightest regions on Pluto are N_2 -rich. Nonetheless, we will continue to consider all five distributions in our effort to fit the thermal data.

For Charon, which has only a shallow visible lightcurve (and for which very little information on the distribution of terrains is available from direct imaging, see Buie et al. 2010b), we assumed a single, H_2O -ice dominated unit. However, we allowed its equivalent geometric albedo to vary as a function of orbital longitude in accordance with the V lightcurve (Buie et al. 2010a). Using a 604 km radius for Charon, precisely determined from stellar occultation (Sicardy et al. 2006), Charon's mean geometric albedo is 0.410, with small (0.392-0.428) orbital variability.

Bolometric albedos required in the thermophysical models are related to geometrical albedos through $A_b = q \times p_V$, where q is the phase integral. Following Lellouch et al. (2000) (and Brucker et al. 2009), who noted the observed correlation between q and p_V on outer planet satellites, we nominally adopted the following values for q : $q = 0.9, 0.8, 0.4$ for units 1, 2, 3 respectively, and $q = 0.6$ for Charon. For a given surface distribution, bolometric albedos were not varied when running the thermophysical model.

An implicit assumption in the above model, also used by Lellouch et al. (2000), is that the local normal albedo is equal to the geometric albedo, and that the spectrally-integrated hemispheric albedo is equal to the bolometric Bond albedo. This is equivalent to assuming that the hemispheric albedo is independent of illumination angle, a reasonable approach in the absence of specific knowledge of the scattering properties of Pluto's and Charon's surfaces.

3.3. Surface roughness description

Surface roughness tends to increase emission temperatures at low emission angles. As outlined in Spencer (1990), these effects depend not only on surface topography (parameterized e.g. by crater shape and coverage, or mean slope angle ($\bar{\theta}$), or rms surface slope) but also to its coupling with subsurface conduction effects (i.e., the Θ parameter). Roughness effects are more pronounced for low Θ values, and decrease to zero in the fast rotator limit ($\Theta = \infty$). They were here included as in our previous study, using the “ $\delta\eta$ ”-approach of Spencer (1990) (see Table IV and Appendix of Lellouch et al. (2000)). Within the framework of an STM, $\delta\eta$ is the difference in the η value caused by surface roughness, i.e. $\delta\eta = \eta_{STM}(\bar{\theta}=0) - \eta_{STM}(\bar{\theta})$. $\delta\eta$ values have been calculated as a function of Θ and surface roughness by Spencer (1990, his Fig. 6). Essentially, we here assumed three roughness cases (“smooth” ($\bar{\theta} = 10^\circ$), “rough” ($\bar{\theta} = 33^\circ$) and “intermediate” ($\bar{\theta} = 20^\circ$)) and used Spencer’s results to calculate a $\eta_{TPM}(\Theta)$ beaming factor appropriate for our thermophysical model, following the method outlined in Lellouch et al. (2000). Results are shown in Fig. 6. These beaming factors can then be incorporated in our thermophysical model, as per Eqn. (2). In what follows, we will generally use the “intermediate” roughness ($\bar{\theta} = 20^\circ$) scenario as the nominal case.

3.4. Special conditions and fitting approach

The above thermophysical model was applied to Charon, and to all Pluto units except the N_2 ice unit. Sublimation–condensation exchanges dominate the heat balance for N_2 , resulting in global isothermality of that ice (e.g. Trafton et al. 1998), so we specified a single temperature for N_2 , constant

over the globe. We assumed $T(\text{N}_2) = 37.4$ K, consistent with a reasonable surface pressure of $15 \mu\text{bar}$ (Lellouch et al. 2009). Using slightly different values for $T(\text{N}_2)$ (e.g. 35 K or 40 K, as in Lellouch et al. 2000) has little impact, since, as discussed below, the contribution of N_2 to the thermal flux is small. Beaming was ignored for N_2 , as is appropriate for an isothermal surface (Spencer 1990). For CH_4 , Stansberry et al. (1996a) demonstrated that sublimation cooling effects become important in the heat budget at temperatures above 54 K. We do not include sublimation terms for CH_4 , but simply account for this effect by imposing a maximum 54 K temperature to the CH_4 unit. The same approach was used by Lellouch et al. (2000), where more discussion can be found on this aspect.

The thermophysical model includes more free parameters (bolometric albedos, bolometric and spectral emissivities, and thermal parameter for each of the Pluto units and Charon) than can be determined from the thermal data, so some of them were fixed a priori or eliminated a posteriori: (i) as previously discussed, bolometric albedos were fixed from fitting of the V lightcurves and our choice of the phase integrals; (ii) for unit 3 (tholin/ H_2O), the bolometric emissivity was always fixed to be 1, and we rejected solutions with spectral emissivities much lower than 1 for that unit, as being implausible for a H_2O -ice dominated unit; (iii) given its low and uniform temperature, N_2 (unit 1) is a small contributor to the thermal emission (negligible at $24 \mu\text{m}$, and $< 10 \%$ of the total flux at $70 \mu\text{m}$), therefore it is not possible to precisely constrain its spectral emissivity; after some trials, we fixed it to be 0.05 at $24 \mu\text{m}$, increasing to 0.5 at $70\text{--}200 \mu\text{m}$ (see Figure 8), broadly consistent with Stansberry et al. (1996b) calculations for N_2 grain sizes of 0.1-0.5

cm (iv) the bolometric and spectral emissivities of unit 2 (CH_4) were free parameters, but we checked internal consistency in the solution parameters, noting that for a Planck function typically peaking near $100\ \mu\text{m}$, the bolometric emissivity should be similar to the spectral emissivity at this wavelength (in contrast, the $24\text{-}\mu\text{m}$ emissivity of CH_4 could be chosen independently of its bolometric emissivity, as the $24\text{-}\mu\text{m}$ flux contributes a negligible amount to the overall radiated energy); and (v) we used a single thermal parameter Θ_{Pl} for units 2 and 3; in other words, the thermal inertia we determine for “Pluto” refers globally to the CH_4 and tholin/ H_2O units. Overall, the fitting approach was rather similar to that of Lellouch et al. (2000), with two noticeable improvements related to Charon: (i) unlike in our previous analysis where Charon’s thermal parameter was assumed ($\Theta_{Ch} = 10$), we here constrained Θ_{Ch} from the $24\ \mu\text{m}$ lightcurve, and (ii) the variation of Charon’s thermal emission with rotation associated with its weak V lightcurve was considered. The spectral and bolometric emissivities for Charon were always assumed to be 1. All thermal models were run with the appropriate geometry for 2004 (sub-observer latitude $\sim 32.9^\circ \sim$ subsolar latitude $\sim 34.5^\circ$).

4. Limits on Charon’s thermal emission

Charon’s mean geometric albedo ($p_V \sim 0.41$) is lower than Pluto’s (~ 0.56). The difference in bolometric albedo should be even more pronounced as a consequence of a likely lower phase integral for Charon compared to Pluto. For equal thermophysical properties (thermal inertia, emissivity), Charon’s surface is therefore expected to be warmer than Pluto. Thus, in spite of its ~ 3.75 times smaller projected area, Charon’s thermal emission may dominate

over Pluto's for sufficiently short wavelengths. This makes the $24\ \mu\text{m}$ data particularly valuable for constraining Charon's thermophysical properties.

Pluto–Charon's minimum flux at $24\ \mu\text{m}$ is $5.71 \pm 0.09\ \text{mJy}$, indicating a maximum of $5.80\ \text{mJy}$ for Charon at this wavelength (equivalent to a maximum $59.42\ \text{K}$ brightness temperature). It can be demonstrated that this implies a non-zero thermal inertia for Charon's surface. Indeed, assuming instantaneous equilibrium with solar input, and ignoring any surface roughness effects (which would only further enhance the flux), the $5.80\ \text{mJy}$ upper limit implies a lower limit of the bolometric Bond albedo of 0.31 . Combined with $p_V \sim 0.41$, this would lead to $q > 0.75$. Such a high value is not realistic given Charon's p_V .

Coming back to our nominal albedo model ($p_V = 0.41$ and $q = 0.6$), the $5.80\ \text{mJy}$ flux upper limit provides a lower limit on the thermal parameter Θ as a function of the assumed surface roughness. Everything else being equal, the larger the surface roughness, the more flux Charon emits, therefore the more stringent the lower limit on Θ will be. We found that the $5.80\ \text{mJy}$ dictates $\Theta_{Ch} > 0.4$, > 1 , > 1.5 and > 2 for the cases of no roughness, small roughness, intermediate roughness and large roughness respectively. Thus a strict lower limit for Charon's thermal inertia is $\Gamma_{Ch} = 2\ \text{MKS}$ ($\Theta_{Ch} > 0.4$); more typically, for intermediate roughness, $\Theta_{Ch} > 1.5$ implies $\Gamma_{Ch} > 7.5\ \text{MKS}$.

Conversely, a lower limit on Charon's $24\ \mu\text{m}$ flux can be obtained by assuming an infinite thermal inertia (rapid rotator), no roughness, and a large phase integral $q \sim 1$, close to Triton's (~ 1.2 , Hillier et al. 1991). In this case, the minimum $24\ \mu\text{m}$ flux from Charon is $0.7\ \text{mJy}$. Altogether, Charon's

24 μm brightness temperature is bracketed between 49.2 K and 59.4 K. Thus, already at this point of the analysis, we can constrain Charon’s mean surface temperature to within ± 5 K (54.3 ± 5.1 K) and prove that Charon is not in instantaneous equilibrium with solar radiation.

5. Fit of the MIPS and IRS data

The above thermophysical model was first applied to fit the MIPS 24, 70 and 160 μm data. As explained before, the free parameters were the thermal parameters for Pluto and Charon (Θ_{Pl} and Θ_{Ch}), and the spectral emissivity of the CH_4 and H_2O /tholin units. The high-quality 24 μm lightcurve was fit first. Essentially, for a given distribution of terrains, the amplitude of this lightcurve constrains Θ_{Pl} , while Θ_{Ch} is determined from the additional “background” flux – actually also somewhat longitude-dependent – required to match the absolute 24 μm fluxes. Results are also sensitive to the (bolometric and spectral) emissivities of the different units. However, as outlined above, the problem is simplified by the facts that (i) the contribution of N_2 to the 24 μm flux is negligible, owing to its low temperature and expected low spectral emissivity (ii) the bolometric and 24 μm emissivity of unit 3 (tholin/ H_2O) is always fixed to 1. Therefore, tunable parameters for fitting the 24 μm lightcurve are essentially Θ_{Pl} , Θ_{Ch} , and $\epsilon(\text{CH}_4)$. Once those were determined, we attempted to fit the 70 and 160 μm data by adjusting the spectral emissivities of units 2 and 3 at those wavelengths. In the entire fitting procedure, we assumed an “intermediate” surface roughness and used the corresponding $\eta_{TPM}(\Theta)$ curve of Fig. 6.

With the above guidelines in hand, we explored parameter space manu-

ally, searching for best fit solutions in a grid with steps of 0.5 for the thermal parameters and 0.05 for the emissivities, and assessing fit quality by eye. The following text, as well as Table 4, give best fit results for the various models and distribution of terrains. We do not provide error bars on the retrieved parameters, as we feel that the true uncertainties are not determined by measurement errors but by model limitations (e.g. the assumed 3-terrain distribution). Rather, exploring parameter space with five different distributions and several emissivity cases should give us a good handle on these uncertainties.

We here detail results obtained with the Lellouch et al. (2000) terrain distribution (g_2), using the geometric albedos for each unit given in Table 3 for that distribution. As it turns out, this distribution provides the best overall match of the *Spitzer* data. Results for the other distributions are then more briefly discussed.

As a starting assumption, we used a bolometric emissivity $\epsilon_{b,CH_4} = 0.855$, taken from Lellouch et al. (2000), and we further assumed $\epsilon_{24\mu m,CH_4} = 1$. With this, a satisfactory match of the 24 μm data was obtained with $\Theta_{Ch} = 3.5$, $\Theta_{Pl} = 6$, although not quite all points were fit within their (small) error bars (Fig. 7, top, green curve). Matching the mean 70 μm 160 μm fluxes then required a decrease of the spectral emissivities of the CH_4 and tholin/water units, typically to 0.7 at 70 μm and 0.5 at 160 μm (green curves in Fig. 7). However, we do not regard this “technical” solution as physically plausible because a constant spectral emissivity of 1 is to be expected for the tholin/water unit and because a 0.5–0.7 spectral emissivity of CH_4 over 70–160 μm is inconsistent with the assumed $\epsilon_{b,CH_4} = 0.855$ bolometric emis-

sivity. We therefore investigated smaller bolometric emissivities for CH_4 , while maintaining $\epsilon_{24\mu\text{m},\text{CH}_4} = 1$. The blue curves in Fig. 7 have $\epsilon_{b,\text{CH}_4} = 0.7$. With $\Theta_{Ch} = 4.5$ and $\Theta_{Pl} = 6$, this now permits a virtually perfect fit of the 24 μm lightcurve, except for the point near $L = 308$, which is perhaps not surprising as the V lightcurve is also not completely well fit over $L = 240\text{--}360$ (Fig. 5).

Continuing with $\epsilon_{b,\text{CH}_4} = 0.7$, and assuming the spectral emissivities shown in Fig. 8, the blue curves in the middle and bottom panel of Fig. 7 show the fits of the 70 and 160 μm data. In both cases, the model somewhat overestimates the mean brightness temperatures from *Spitzer/MIPS*. Furthermore, a significant mismatch of the 70 μm data occurs at $L \sim 80$ and $L \sim 307$, where the anomalously low T_B s cannot be fit with the model. In contrast, the model follows more closely the shape of the *ISO* 60 μm lightcurve. In this sense, it provides a compromise between the *Spitzer*-derived 70 μm and *ISO*-derived 60 μm T_B s and we regard it as satisfactory. Note also that forcing the model to match the mean *Spitzer/MIPS* 70 and 160 μm brightness temperatures would require $\epsilon_{70\mu\text{m},\text{CH}_4} \sim 0.5$ and $\epsilon_{160\mu\text{m},\text{CH}_4} \sim 0.2$, which we regard as implausible and inconsistent with $\epsilon_{b,\text{CH}_4} = 0.7$.

Finally, we also investigated the effect of assuming a low 24- μm emissivity for CH_4 ice. This situation may in fact be expected, according to Stansberry et al. (1996b)'s emissivity calculations based on Hapke theory (Hapke 1993). For definiteness, we used here $\epsilon_{24\mu\text{m},\text{CH}_4} = 0.35$, corresponding to their results for mm-sized CH_4 grains. With the considered terrain distribution, this assumption (red curve in the top panel of Fig. 7) leads however to a strong lack of flux in the longitude range thermally dominated by CH_4 , i.e. over

$L = 250\text{--}50$ (see Fig. 4). On this basis, this low emissivity is rejected. In summary our preferred model follows the emissivity curves of Fig. 8.

Once the model was tuned in this manner to the MIPS data, it was applied to the IRS spectra at the appropriate longitudes (Fig. 9, top). Overall, the $21\text{--}37\text{ }\mu\text{m}$ spectra are well matched, and the general decrease of T_B with increasing λ properly captured. This decrease is due to a combination of two effects (i) the mixing of Planck functions at different temperatures naturally produces a decrease of the mean T_B with λ (ii) the decrease of ϵ_{λ, CH_4} with λ . The bottom part of Fig. 9 shows the extension of the model to the entire $20\text{--}200\text{ }\mu\text{m}$ range. Again, the overall behaviour is well explained, at least up to $\sim 100\text{ }\mu\text{m}$. At longer wavelengths, the ISO (150 and $200\text{ }\mu\text{m}$) and MIPS ($160\text{ }\mu\text{m}$) do not provide a consistent picture, and the model appears to present a compromise between the different datasets.

Figure 9, which displays the model brightness temperatures for the *Spitzer* observing conditions of 2004, presents only an approximate assessment of the model ability to match the ISO observations taken in 1997. Indeed, in Fig. 9, the ISO T_B s are simply corrected to the 2004 heliocentric distance (according to $R_h^{-1/2}$), without any possible correction for the different observing geometry (i.e. the subsolar latitude β). In Fig. 10, we re-calculate the expected ISO 60- and $100\text{-}\mu\text{m}$ lightcurves by rigorously applying the model to the ISO observing conditions, i.e. $R_h = 29.95\text{ AU}$ and $\beta = 19^\circ$. The spectral emissivities of the various units are still taken from Fig. 8. Comparison to the actual ISO measurements indicates very satisfactory agreement at $60\text{ }\mu\text{m}$, comparable to the optimum fits of the ISO data (see Fig. 12 in Lellouch et al. 2000). At $100\text{ }\mu\text{m}$, the model slightly overestimates (by about

1 K) the ISO-derived T_{BS} , fully consistent with the fact that Lellouch et al. (2000) achieved their best fits by adjusting upwards the calibration of the ISO 100 μm fluxes by 10 %. We conclude that our best fit model permits a simultaneous fit of all data from ~ 20 to $\sim 100 \mu\text{m}$ taken in 1997 and 2004.

Given the overall low quality of the available data longward of 100 μm , however, we did not attempt to constrain the spectral emissivities there. Much improved observations are needed to validate the model in this spectral range. They could be obtained from combined *Herschel*-PACS (at 70, 100, 160 μm , Poglitsch et al. 2010) and SPIRE (at 250, 350, 550 μm , Griffin et al. 2010) lightcurve measurements. Note that the model spectra at the different longitudes are not “parallel” and occasionally cross over. This is the consequence of the decrease of the spectral emissivity of CH_4 and its variable surface coverage. If the present model is valid, *Herschel* lightcurves in different filters are predicted to be somewhat out of phase; PACS and SPIRE lightcurve data could therefore provide a sensitive test of our emissivity conclusions.

The same approach was used for the other four distributions of terrains. Table 4 summarizes the best fit parameters (Θ_{Pl} , Θ_{Ch} , and the 70 μm emissivity of the CH_4 and tholin/ H_2O units). As previously, a bolometric emissivity of 1 for tholin/ H_2O was assumed, and the models were run for the two values of the CH_4 bolometric emissivity, 0.855 and 0.7; in the latter case, the two values for the CH_4 24 μm emissivity (1 and 0.35) were tested.

Fig. 11 compares fit quality of the 24- μm data for the 5 distributions and the various emissivity cases. The top two panels of Fig. 11 have $\epsilon_{24\mu\text{m},\text{CH}_4} = 1$. They show that for either $\epsilon_{b,\text{CH}_4} = 0.855$ or $\epsilon_{b,\text{CH}_4} = 0.7$, distributions g₃

(“Modified Grundy and Fink”) and b_1 (“Sliced-HST”) give poor fits to the 24- μm data lightcurve, while the other three distributions provide a satisfactory match. Furthermore, as indicated in Table 4 and discussed above for distribution g_2 , assuming a high bolometric emissivity for CH_4 (0.855) implies 70 μm spectral emissivities of ~ 0.7 or less for the CH_4 and tholin/ H_2O units, inconsistent with their assumed ϵ_b . The last column of Table 4 comments on fit quality and/or solution inconsistencies. For the family of models with $\epsilon_{24\mu\text{m},\text{CH}_4} = 1$, three distributions (g_1 , g_2 and b_3) provide satisfactory fits, each time having $\epsilon_{b,\text{CH}_4} = 0.7$. The first two provide very consistent solutions as for the thermal parameter of Pluto and Charon ($\Theta_{Pl} = 4.5$, $\Theta_{Ch} = 5-6$). In contrast, the best fit for distribution b_3 indicates rather different values for Θ , especially for Charon ($\Theta_{Pl} = 7.5$, $\Theta_{Ch} = 30$). This stems primarily from the larger and longitudinally more homogeneous coverage of the (tholin/ H_2O) unit 3 in distribution b_3 (32 % of the surface) compared to g_1 and g_2 (7 % and 14 %): fitting the 24- μm lightcurve amplitude and mean level with distribution b_3 requires somewhat less warm temperatures of unit 3 and especially a reduced Charon contribution (about 1.65 mJy, vs 3.15 mJy in the case of distribution g_1 , see Fig. 12). Note however that fitting the 70- μm data with this distribution implies a very low (0.3) spectral emissivity of CH_4 at this wavelength, inconsistent with the assumed $\epsilon_{b,\text{CH}_4} = 0.7$.

Distributions g_3 , b_1 and b_3 have more extended tholin/ H_2O patches than others. Therefore, the 24- μm fluxes in these three cases are somewhat less sensitive to $\epsilon_{24\mu\text{m},\text{CH}_4}$ than for other distributions, and as shown in the bottom panel of Fig. 11, a reasonable match of the 24- μm lightcurve can be obtained for $\epsilon_{24\mu\text{m},\text{CH}_4} = 0.35$ with distribution g_3 (unlike was the case of distribution

g_2). Note that in no case does the “sliced-HST” scenario (b_1) provide an acceptable match of the MIPS data. In addition, as noted before, matching the HST lightcurve with this distribution leads to a higher albedo for CH_4 than for N_2 . For the two reasons, we reject this distribution.

6. Discussion and conclusions

As is probably clear from the above description, the complexity of the problem, including ambiguities in surface albedo maps and the number of parameters impacting the thermal emission, makes it rather difficult to retrieve all of them in a unique manner. Nonetheless, our exploration of parameter space and inspection of fit quality (Table 4, Figs. 7 and 11) suggest several trends warranting discussion.

6.1. Surface emissivities

Determining the bolometric and spectral emissivities of the four units of our model independently does not appear possible. Hence our approach has consisted of fixing the emissivities of all of them except one. Given the absorption properties of H_2O ice in the far-infrared we assumed a constant emissivity of 1 for units containing water ice, i.e. Charon and the tholin/ H_2O unit on Pluto. As N_2 is a small contributor to the overall thermal emission, due to its low temperature, we specified the (spectrally-variable) emissivity for the N_2 unit, instead of trying to determine it. With this approach, the only adjustable emissivities were those of the CH_4 unit.

The emissivity behaviour shown in Fig. 8 is reasonably but not completely consistent with expectations based on the spectral properties of ices

in the far-infrared. First, the adopted spectral emissivity for N_2 , increasing with λ from 0.05 at $24\ \mu\text{m}$ to 0.5 at $70\text{--}200\ \mu\text{m}$, roughly corresponds to Stansberry et al.'s (1996b) predictions for N_2 grain sizes of 0.1-0.5 μm . Based on the modelling of near-IR spectra, grain sizes for the N_2 -dominated unit on Pluto are rather 5-10 μm (Grundy and Fink 1996, Douté et al. 1999, Olkin et al. 2007, Protopapa et al. 2008); for this size range, much larger emissivities for N_2 (0.95-1) are expected based on Stansberry et al.'s (1996b) results. We note that they based their calculations on absorption coefficients by Buontempo et al. (1979), while more recent experiments (Winnewisser et al. 1989, as well as additional measurements reported in Lellouch et al. 2000) indicate factor-of-2 lower absorption. Nonetheless, even a factor-of-2 on the absorption coefficient has a small impact on the derived emissivities (e.g. $\sim 5\%$ on the bolometric emissivity). On the other hand, with our adopted spectral emissivities for N_2 , the Planck-mean bolometric emissivity is about 0.5, typical of values used in ice evolution models on Triton or Pluto (Spencer and Moore 1992, Hansen and Paige 1992, 1996).

The adopted N_2 emissivities have no impact on the $24\ \mu\text{m}$ fits, as the N_2 contribution is entirely negligible at this wavelength. Based on a variety of models (see Table 4 and Fig. 11), we find that large spectral emissivities for CH_4 (i.e. $\epsilon_{24\mu\text{m},CH_4} = 1$) generally provide better fits to these data (especially over $L = 250\text{--}50$) than lower values (e.g. $\epsilon_{24\mu\text{m},CH_4} = 0.35$) do; one exception to this is for the modified Grundy and Fink distribution (g_3). This is surprising in view of the calculations of Stansberry et al. (1996b), who find the CH_4 $24\ \mu\text{m}$ emissivity to be significantly lower than 1 for a broad range of grain size. In addition, the $70\ \mu\text{m}$ lightcurves (and tentatively the

fluxes at longer wavelengths) indicate a decrease of the CH_4 emissivity with wavelength, with an overall bolometric emissivity of ~ 0.7 , lower than estimated previously from the ISO data. Estimated grain sizes for the pure CH_4 unit vary wildly, ranging from $200\ \mu\text{m}$ (Olkin et al. 1997) to $500\text{--}1500\ \mu\text{m}$ (Douté et al. 1999) or even $0.1\ \text{mm} - 1\ \text{cm}$ (Grundy and Buie 2001) or $2\ \text{mm} - 6\ \text{cm}$ (Merlin et al. 2010). The emissivity curve we derive for CH_4 is not matched by a single grain size in the Stansberry et al. calculations. Emissivities of $0.7\text{--}0.5$ over $70\text{--}200\ \mu\text{m}$ are consistent with grain sizes of $1\ \text{mm}$, in good agreement with Douté et al. (1999), but larger emissivities at lower wavelengths are not easily explained except for very large ($> 5\ \text{cm}$) CH_4 grains. Note finally that adopting larger N_2 emissivities (e.g. following Stansberry et al. 1996b predictions for $5\text{--}10\ \text{cm}$ grains) would have led to an even steeper decrease of the CH_4 emissivity with λ . All these aspects point to the difficulty of predicting ice emissivities based on Hapke theory using a single particle size.

6.2. Thermal inertia

Columns 5 and 6 in Table 4 summarize the thermal parameters derived for Pluto (Θ_{Pl}) and Charon (Θ_{Ch}) for the various distributions of terrains and CH_4 emissivity cases. For Pluto, the overall range indicated in Table 4 is $\Theta_{Pl} = 4\text{--}12$, but only the $\Theta_{Pl} = 5\text{--}8$ range provides good or acceptable fits. For Charon the range of thermal parameters is broader ($\Theta_{Ch} = 2.5\text{--}30$), but most of the solutions encompass a much smaller range ($\Theta_{Ch} = 2.5\text{--}4.5$). Only distribution b_3 leads to high Θ_{Ch} values. As this distribution implies an anomalously low $70\ \mu\text{m}$ emissivity (0.3) for CH_4 and a relatively poor fit of the HST V lightcurve of Buie et al. (2000a), it may be tempting to discard

it. However, this distribution, in which the different components are mixed on small scales, might instead be regarded as a more realistic representation of the complexity of Pluto's surface, and was actually designed to achieve a closer match to the HST/WFPC2 1994 images. We therefore do not exclude the high Θ_{Ch} values, simply noting that small values of 2.5-4.5, achieved for the best-fit models (g_1, g_2, g_3), are preferred.

The relationship between thermal inertia Γ and the thermal parameter Θ (Eq. 1) involves the surface bolometric emissivity ϵ_b and the instantaneous equilibrium sub-solar temperature T_{SS} . Taking a mean $\epsilon_b = 0.85$ and $A_b = 0.46$ for Pluto (obtained for $p_V = 0.58$ and $q = 0.8$), we obtain $T_{SS} = 63.3$ K at the 30.84 AU heliocentric distance. This gives $\Gamma_{Pl} = 20\text{--}30$ J m⁻² s^{-1/2} K⁻¹. For Charon (taking $\epsilon_b = 1$, $p_V = 0.41$, $q = 0.6$), $T_{SS} = 66.1$ K. With this, we obtain $\Gamma_{Ch} = 10\text{--}150$ J m⁻² s^{-1/2} K⁻¹ for Charon (using the full range $\Theta_{Ch} = 2.5\text{--}30$), with $\Gamma_{Ch} = 10\text{--}20$ J m⁻² s^{-1/2} K⁻¹ as the preferred range. These thermal inertias refer to surface layers comparable to the diurnal skin depth, i.e. as detailed below the first few centimeters of the surface.

The 20–30 MKS thermal inertia we infer for Pluto is consistent with, but considerably more accurate than, values previously found from the ISO data (15–100 MKS, Lellouch et al. 2000), while the value for Charon is a first determination. The range of Charon 24 μ m fluxes covered by the model solutions (1.6-4.5 mJy) indicates a mean surface temperature of 55.4 ± 2.6 K. This is to be compared with results from millimeter-wave interferometry resolving the Pluto-Charon pair, indicating 1.4 mm brightness temperatures of 37 ± 2.5 K for Pluto and 49 ± 8 K for Charon, i.e. physical temperatures of 41 ± 3 and

54 ± 9 K, assuming a 1.4 mm emissivity of 0.9 (Gurwell et al. 2010). Thus, although the *Spitzer* observations do not isolate Charon from Pluto, they appear to provide a much improved constraint on Charon’s surface temperature. We also note that our mean Charon temperature is consistent with, and again much more accurate than, temperatures inferred from the shape of the H_2O ice 1.6–1.7 μm feature in Charon’s spectrum (60 ± 20 K, Buie and Grundy 2000; 42–53 K with a 5–10 K accuracy, Cook et al. 2007).

The thermal inertias of Pluto and Charon are much less than values expected for compact ices at ~ 40 K, typically 500 MKS for N_2 , CH_4 and CO and 2000 MKS for H_2O (Spencer et al. 1997). This indicates a poor thermal conductivity, probably resulting from high surface porosity and poor surface consolidation. The Pluto values are intermediate between the thermal inertias of Saturn’s satellites (9–20 MKS; Howett et al. 2010) and those of Jupiter’s satellites (50–70 MKS; Spencer 1987, Spencer et al. 1999, Rathbun et al. 2003). As discussed in Howett et al. (2010), why Saturn’s satellites appear to have smaller thermal inertias than Jupiter’s is not readily understood, though possible explanations include (i) the higher gravity on Jupiter’s satellites, resulting in a somewhat higher surface consolidation (ii) the coating of Saturn’s satellites by fine E-ring material (Verbiscer et al. 2007), producing a highly porous surface. Interestingly, the surface gravity of Pluto (and Charon) is intermediate between those of Jupiter’s and Saturn’s satellites. In addition, laboratory experiments (see Douté et al. 1999) show that atmospheric sublimation cycles should lead to the formation of small, weakly bound, pure CH_4 grains, with porous snow-like structure, and that the irradiation of methane ice is also expected to produce fine-grained

organic materials with lower conductivity than pure ices. Therefore, a porous surface on Pluto with low thermal inertia is probably not surprising. We here re-iterate that the thermal inertia determined for Pluto refers to the CH_4 and tholin/ H_2O units. In contrast, given the large ($\sim\text{cm}$) N_2 grain size, which likely reflects the evolution of the sublimating deposits into large, compact, polycrystalline grains, the N_2 -dominated unit is expected to have a large thermal inertia.

Though not entirely conclusive, our results also suggest that Charon's thermal inertia is smaller than Pluto's. The ~ 2 times smaller gravity on Charon may play a role in an even less consolidated upper surface than on Pluto. In possible relation to this, Pluto and Charon show different behaviours of their phase curves (Buie et al. 2010a). Down to phase angles of 0.3° , Pluto's phase curve is linear, while Charon's exhibits a clear departure from linearity, and a strong and broad opposition surge, attributable to coherent backscattering (Buie et al. 2010c). Another explanation of the possibly different thermal inertia of Pluto and Charon could be that heat conduction on a porous surface is assisted by atmospheric conduction within the pores (Spencer and Moore 1992). Using plausible values for grain and pore sizes (typically several mm), Pluto's $\sim 15 \mu\text{bar}$ atmosphere may significantly contribute to the effective thermal conduction of its upper surface (Lellouch et al. 2000).

Thermal observations of many other TNOs have been performed by *Spitzer* (Stansberry et al. 2008) and are currently underway by *Herschel* (Müller et al. 2010, Lellouch et al. 2010a). Due to far less detailed knowledge of these objects (with often no information on rotation parameters and even

less on possible surface heterogeneity), thermal modelling of the observations is usually performed by assuming homogeneous bodies and in the standard NEATM/STM formalism, with the η ($=\eta_{STM}$) parameter empirically characterizing the temperature distribution across their surfaces. Model fits generally require η values slightly in excess of unity (e.g. $\eta = 1.2 \pm 0.35$, Stansberry et al. 2008). Such values appear comparable to those found on near-Earth asteroids (Wolters et al. 2008), which have high thermal inertias ($200 \pm 40 \text{ J m}^{-2} \text{ s}^{-1/2} \text{ K}^{-1}$, Delbo' et al. 2007). However, given the much colder temperatures in the Kuiper Belt, the measured η there are instead indicative of low surface inertias combined with important roughness effects. While Pluto, with an active atmosphere ultimately responsible for its variegated appearance, is a somewhat unique case, it is instructive to compare our findings for Charon to those found on some of its siblings, particularly the two H_2O ice-covered and large objects 90482 Orcus and 136108 Haumea. In the NEATM formalism, Charon's 24 mJy fluxes corresponding to the preferred $\Gamma_{Ch} = 10 - 20 \text{ J m}^{-2} \text{ s}^{-1/2} \text{ K}^{-1}$ values would be obtained for $\eta = 1.21 - 1.40$. This is very similar to the η inferred from Haumea's thermal lightcurve (1.15–1.35, Lellouch et al. 2010b), and somewhat higher than the value for Orcus ($\eta = 0.97 \pm 0.07$, Lim et al. 2010). To first order, similar η values indicate similar values of the thermal parameter Θ , but this similarity cannot be extrapolated to Γ . From Eq. (1), Γ / Θ is proportional to $(\tau/R_h^3)^{1/2}(1 - A_b)^{3/4}$ and τ is the rotation period. Putting numbers, the f factor is ~ 18 (resp. 6.5) times larger for Charon than it is for Haumea (resp. Orcus), due essentially to the much longer rotation period and smaller R_h for Charon. This rough scaling leads to Γ of order 0.5–3 MKS for Haumea and Orcus;

for the latter, this estimate agrees with the thermophysical modelling presented in Lim et al. (2010). Thus, unless they have extremely large surface roughness, the conclusion that these two large, water-ice dominated bodies have extremely low thermal inertia seems unescapable. Low thermal inertia (< 10 MKS) is also observed on the largest main-belt asteroids ($D > 200$ km) and interpreted as due to their ability of maintaining a fine, thermally insulating regolith layer (Delbo' and Tanga 2009). In contrast, as exemplified by the above values for the outer planet satellites, such thermal inertias are not observed on icy bodies in this size regime.

The ~ 1 order of magnitude difference in thermal inertia between Charon on the one hand, Orcus and Haumea on the other hand, can probably be interpreted in terms of a different skin depth d , i.e. the depth into the surface probed by thermal emission. The skin depth is expressed as $d = \sqrt{k/\rho c \omega} = \Gamma/(\rho c \sqrt{\omega})$, where $\omega = 2\pi/\tau$, ρ is the density, c is the heat capacity and k is the thermal conductivity. Using a typical $\rho = 930$ kg m $^{-3}$ and $c = 350$ J kg $^{-1}$ K $^{-1}$ for H $_2$ O ice at ~ 40 K (Spencer et al. 1997), this gives nominally $d \sim 1.5$ cm for Charon, but only 0.5 mm for Orcus and 0.1 mm for Haumea. Therefore, the extremely low thermal inertia for Orcus and Haumea may reflect the fluffiest material in the upper millimeter of the surface, while the low, yet more moderate, thermal inertia determined for Charon may represent somewhat more compacted and conductive material ~ 1 cm below the surface. An analogy is perhaps to be found with the behaviour of lunar regolith, showing rapidly increasing thermal conductivity with depth (Keihm et al. 1973). Recent mm/submm thermal measurements at asteroid 21 Lutetia indicate a similar gradient of thermal conductivity over the first centimeters

of the surface (Gulkis et al., to be submitted).

Additional *Spitzer*-MIPS data were obtained on April 8-14, 2007 (24 and 70 μm), September 19-20, 2007 (160 μm) and October 20-26, 2008 (mostly 160 μm). The detailed description of these observations will be published elsewhere. However, we note that compared to the observations from 2004, the April 2007 data reveal a fading of the Pluto-Charon system (Stansberry et al. 2009), with a decrease of the 24 μm (resp. 70 μm) brightness temperatures by ~ 0.5 K (resp. ~ 2 K). Taking our model fit to the 2004 data and accounting for the changes in distance and viewing geometry for the April 2007 epoch (i.e. $R_h = 31.27$ AU and $\beta = 39^\circ$), we find that the decrease in Pluto-Charon's brightness is not due to the change in observing circumstances alone (Fig. 13). Qualitatively, this suggests changes in ice distribution and/or surface albedos over 2004-2007; for example, an extension of N_2 ice coverage in the sunlit regions would result in a dimming of Pluto in the thermal range. Unfortunately, no published optical (lightcurve or imaging) data are available to confirm changes over this time frame, though near-infrared spectra provide indications of secular changes in Pluto's surface composition (Grundy et al. 2009). Modelling and interpretation of these more recent *Spitzer* data as well as of early Pluto observations obtained by *Herschel* in September 2009 and March 2010 is deferred to a later publication.

In the very near future, spatially-resolved temperature measurements on Pluto's and Charon's disks will be possible, using the mapping capabilities of ALMA at submillimeter wavelengths (Mouillet et al. 2011). It is certainly unfortunate that the *New Horizons* spacecraft, scheduled to visit the Pluto system in July 2015, does not carry any thermal infrared instrument.

Nonetheless, indirect temperature measurements should be obtained on N₂, CH₄ and H₂O ices from near-infrared band shapes observed with the Ralph instrument (Reuter et al. 2008). A particularly promising aspect will be the investigation of diurnal surface temperature variations, as the most direct way to determine the thermal inertias of the various compositional units.

References

- Brucker, M.J., Grundy, W.M., Stansberry, J.A., Spencer, J.R., Sheppard, S.S., Chiang, E.I., Buie, M.W., 2009. High albedos of low inclination Classical Kuiper belt objects. *Icarus* 201, 284–294.
- Buie, M.W., Grundy, W.M., 2000. The distribution and physical State of H₂O on Charon. *Icarus*, 148, 324–339.
- Buie, M.W., Tholen, D.J., Horne, K., 1992. Albedo maps of Pluto and Charon. Initial mutual event results. *Icarus* 97, 211–227.
- Buie, M.W., Tholen, D.J., Wasserman, L.H., 1997. Separate lightcurves of Pluto and Charon, *Icarus* 125, 233–244.
- Buie, M.W., Grundy, W.M., Young, E.F., Young, L.A., Stern, S.A., 2010a. Pluto and Charon with the Hubble Space Telescope. I. Monitoring Global Change and Improved Surface Properties from light curves. *Astron. J.* 139, 1117–1127.
- Buie, M.W., Grundy, W.M., Young, E.F., Young, L.A., Stern, S.A., 2010b. Pluto and Charon with the Hubble Space Telescope. II. Resolving changes on Pluto's surface and a map for Charon. *Astron. J.* 139, 1128–1143.
- Buie, M.W., Grundy, W.M., Tholen, D.J., Stephens, D.C., 2010c. Photometric properties of the Pluto system. *Bull. Amer. Astron. Soc.*, 42, 983.
- Buontempo, U., Cunsolo, S., Dore, P., Maselli, P., 1979. Far infrared absorption spectra of β -solid nitrogen. *Phys. Lett.* 74A, 113–115.
- Cook, J.C., Desch, S.J., Roush, T.L., Trujillo, C.A., Geballe, T.R., 2007. Near-infrared spectroscopy of Charon: possible evidence for cryovolcanism on Kuiper Belt objects. *Astrophys. J.* 663, 1406–1419.
- Delbo', M., Tanga, P., 2009. Thermal inertia of main belt asteroids smaller

- than 100 km from IRAS data. *Planet. Space Sci.* 57, 259–265.
- Delbo', M., DellOro, A., Harris, A.W., Mottola, S., Mueller, M., 2007. Thermal inertia of near-Earth asteroids and implications for the magnitude of the Yarkovsky effect, *Icarus* 190, 236249.
- Douté, S., Schmitt, B., Quirico, E., Owen, T.C., Cruikshank, D.P., de Bergh, C., Geballe, T.R., Roush, T.L., 1999. Evidence for methane segregation at the surface of Pluto. *Icarus* 142, 421-444.
- Engelbracht, C.W., et al., 2007. Absolute calibration and characterization of the multiband imaging photometer for Spitzer. I. The stellar calibrator sample and the 24 μm calibration. *Publ. Amer. Soc. Pacific* 119, 994–1018.
- Gordon, K.D., et al., 2007. Absolute calibration and characterization of the multiband imaging photometer for Spitzer. I. 70 μm imaging. *Publ. Amer. Soc. Pacific* 119, 1019–1037.
- Griffin, M.J., et al., 2010. The Herschel-SPIRE instrument and its in-flight performance. *Astron. Astrophys.* 518, DOI: 10.1051/0004-6361/201014717.
- Grundy, W.M., Buie, M.W., 2001. Distribution and evolution of CH_4 , N_2 , and CO ices on Pluto's Surface: 1995 to 1998. *Icarus* 153, 248–263.
- Grundy, W.M., Buie, M.W., 2002. Spatial and compositional constraints on non-ice components and H_2O on Pluto's surface. *Icarus* 157, 128–138.
- Grundy, W.M., Fink, U. 1996. Synoptic CCD spectrophotometry of Pluto over the past 15 years. *Icarus* 124, 329–343.
- Grundy, W.M., Young, L.A., Olkin, C.B., Buie, M.W., Stansberry, J.A., 2009. Observed spatial distribution and secular evolution of ices on Pluto and Triton. *Bull. Amer. Astron. Soc.* 41, 06.01
- Gurwell, M.A., Butler, B.J., 2005. Sub-arcsecond scale imaging of the

- Pluto/Charon binary system at 1.4 mm. *Bull. Amer. Astron. Soc.* 37, 55.01
- Gurwell, M.A., Butler, B.J., Moullet, A., 2010 Subarcsecond scale imaging of the Pluto-Charon system at 1.1 and 1.4 mm. *Bull. Amer. Astron. Soc.* 42, 33.03
- Hansen, C.J., Paige, D.A., 1992. A thermal model for the seasonal nitrogen cycle on Triton. *Icarus* 99, 273–288.
- Hansen, C.J., Paige, D.A., 1996. Seasonal nitrogen cycles on Pluto. *Icarus* 120, 247–265.
- Hapke, B.W., 1983. *Theory of Reflectance and Emittance Spectroscopy*. Cambridge University Press, Cambridge, 1993.
- Harris, A.W., 1998. A thermal model for near-Earth asteroids. *Icarus* 131, 291–301.
- Howett, C.J.A., Spencer, J.R., Pearl, J., Segura, M., 2010. Thermal inertia and bolometric Bond albedo values for Mimas, Enceladus, Tethys, Dione, Rhea and Iapetus as derived from Cassini/CIRS measurements. *Icarus* 206, 573–593.
- Hillier, J., Helfenstein, P., Verbiscer, A., Veverka, J., 1991. Voyager photometry of Triton. Hazes and surface photometric properties. *J. Geophys. Res.*, 96, 19203–19209.
- Houck, J., et al., 2004. The Infrared Spectrograph on the Spitzer Space Telescope. *Astrophys. J. Sup. Ser.* 154, 18–24.
- Keihm, S.J., Peters, K., Langseth, M.G., Chute, J.L., Jr., 1973. Apollo 15 measurements of lunar surface brightness temperatures. Thermal conductivity of the upper 1 1/2 meters of regolith. *Earth Planet. Sci. Lett.* 19, 337–351.

- Lacerda, P., Jewitt, D., Peixinho, N., 2008. High-precision photometry of extreme KBO 2003 EL61. *Astron. J.* 135, 1749–1756. (Erratum in *Astron. J.* 136, 1754).
- Lellouch, E., Laureijs, R., Schmitt, B., Quirico, E., de Bergh, C., Crovisier, J., Coustenis, A., 2000. Pluto’s non-isothermal surface. *Icarus* 147, 220–250.
- Lellouch, E., Stansberry, J., Cruikshank, D., Grundy, W., 2006a. Pluto’s thermal lightcurve: Spitzer MIPS observations. International Workshop on “Trans-Neptunian objects dynamical and physical properties”, Catania, 3-7 July 2006.
- Lellouch, E., Stansberry, J., Cruikshank, D., Emery, J., Grundy, W., 2006b. Pluto’s thermal Lightcurve: Spitzer MIPS and IRS observations. *Bull. Amer. Astron. Soc.* 38, 21.04
- Lellouch, E., Sicardy, B., de Bergh, C., Käufl, H.-U., Kassi, S., Campargue, A., 2009. Pluto’s lower atmosphere structure and methane abundance from high-resolution spectroscopy and stellar occultations. *Astron. Astrophys.*, 495, L17-L21.
- Lellouch, E., Müller, T., TNOs are cool team, 2010a, Planetary Results from the Herschel Mission Part II: TNO’s are Cool! *Bull. Amer. Astron. Soc.*, 42, 35.04.
- Lellouch, E., et al., 2010b. “TNOs are cool”: A survey of the trans-Neptunian region. II. The thermal lightcurve of (136108) Haumea. *Astron. Astrophys.* 518, DOI: 10.1051/0004-6361/201014648.
- Lim, T., et al., 2010. “TNOs are Cool”: A survey of the trans-Neptunian region. III. Thermophysical properties of 90482 Orcus and 136472 Make-

- make. *Astron. Astrophys.* 518, DOI: 10.1051/0004-6361/201014701.
- Merlin, F., Barucci, M.-A., de Bergh, C., DeMeo, F.E., Alvarez-Candal, A., Dumas, C., Cruikshank, D.P. 2010. Chemical and physical properties of the variegated Pluto and Charon surfaces. *Icarus* 210, 930–943.
- Moulet, A., Lellouch, E., Moreno, R., Gurwell, M. Physical studies of centaurs and Trans-Neptunian objects with the Atacama Large Millimeter Array. *Icarus*, 213, 382–392.
- Müller, T. et al., 2010. “TNOs are Cool”: A survey of the trans-Neptunian region. I. Results from the Herschel science demonstration phase (SDP). *Astron. Astrophys.* 518, DOI: 10.1051/0004-6361/201014683.
- Olkin, C.B., Young, E.F., Young, L.A., Grundy, W., Schmitt, B., Toku-naga, A., Owen, T., Roush, T., Terada, H. 2007. Pluto’s spectrum from 1.0 to 4.2 μm : implications for surface properties. *Icarus* 133, 420–431.
- Poglitsch, A., et al., 2010. The Photodetector Array Camera and Spec-trometer (PACS) on the Herschel Space Observatory. *Astron. Astrophys.* 518, DOI: 10.1051/0004-6361/201014535.
- Protopapa, S., Boehnhardt, H., Herbst, T.M., Cruikshank, D.P., Grundy, W.M., Merlin, F., Olkin, C.B., 2008. Surface characterization of Pluto and Charon by L and M band spectra. *Astron. Astrophys.* 490, 365–375.
- Rathbun, J., Spencer, J., Tamppari, L., Martin, T., Bernard, L., Travis, L., 2003. Mapping of Ios thermal radiation by the Galileo Photopolarime-terRadiometer (PPR) instrument, *Icarus* 169, 127–139.
- Reuter, D.C., et al., 2008. Ralph: a visible/infrared imager for the New Horizons Pluto/Kuiper Belt mission. *Space Sci. Rev.*, 140, 129–154.
- Rieke, G.H., Young, E.T., Engelbracht, C.W., Kelly, D.M., Low, F.J.,

- and 38 co-authors, 2004. The Multiband Imaging Photometer for Spitzer (MIPS). *Astrophys. J. Suppl.* 154, 25-29.
- Schaefer, B.E., Buie, M.W., Smith, L.T., 2008. Pluto's light curve in 1933–1934. *Icarus*, 197, 590–598.
- Sicardy, B., et al., 2006. Charon's size and an upper limit on its atmosphere from a stellar occultation *Nature* 439, 52–54.
- Spencer, J., 1987. The surfaces of Europa, Ganymede, and Callisto: an investigation using Voyager IRIS thermal infrared spectra. PhD thesis, University of Arizona.
- Spencer, J.R., 1990. A rough-surface thermophysical model for airless planets. *Icarus*, 83, 27–38.
- Spencer, J., Moore, J.M., 1992. The influence of thermal inertia on temperatures and frost stability on Triton. *Icarus* 99, 261–272.
- Spencer, J., Lebofsky, L., Sykes, M., 1989. Systematic biases in radiometric diameter determinations, *Icarus* 78, 337-354.
- Spencer, J.R., Stansberry, J.A., Trafton, L.M., Young, E.F., Binzel, R.P., Croft, S.K., 1997. Volatile transport, seasonal cycles and atmospheric dynamics on Pluto. In "Pluto and Charon" (S.A. Stern and D.J. Tholen, Eds.), 435–475. University of Arizona Press, Tucson.
- Spencer, J., Tamppari, L., Martin, T., Travis, L., 1999. Temperatures on Europa from Galileo PPR: nighttime thermal anomalies. *Science* 284, 1514–1516.
- Stansberry, J.A., Spencer, J.R., Schmitt, B., Benchkoura, A.-I., Yelle, R.V., Lunine, J.I., 1996a. A model for the overabundance of methane in the atmospheres of Pluto and Triton Planet. *Space Sci.* 44, 1051–1063.

- Stansberry, J.A., Pisano, D.J., Yelle, R.V., 1996b. The emissivity of volatile ices on Triton and Pluto Planet. Space Sci. 44, 945–955.
- Stansberry, J.A., Grundy, W.M., Margot, J.L., Cruikshank, D.P., Emery, J.P., Rieke, G.H., Trilling, D.E., 2006. The albedo, size, and density of binary Kuiper Belt object (47171) 1999TC36. *Astrophys. J.* 643, 556–566.
- Stansberry, J.A., et al., 2007. Absolute Calibration and Characterization of the Multiband Imaging Photometer for Spitzer. III. An Asteroid-based Calibration of MIPS at 160 μm . *Publ. Amer. Soc. Pacific*, 119, 1038–1051.
- Stansberry, J., Grundy, W., Brown, M., Cruikshank, D., Spencer, J., Trilling, D., Margot, J.-L., 2008. Physical Properties of Kuiper Belt and Centaur Objects: Constraints from the Spitzer Space Telescope. In “The Solar System Beyond Neptune”, M.A. Barucci, H. Boehnhardt, D. P. Cruikshank, and A. Morbidelli (eds.), University of Arizona Press, Tucson.
- Stansberry, J.A., Lellouch, E., Grundy, W., Hicks, M., Buie, M., Young, L., 2009. Pluto’s changing surface in the far-IR. *Bull. Amer. Astron. Soc.*, 41, 06.02.
- Stansberry, J.A., Grundy, W., Mueller, M., Benecchi, S.D., Rieke, G.H., Noll, K.S., Buie, M.W., Levison, H.F., Porter, S.B., Roe, H.G., 2011. Physical Properties of Trans-Neptunian Binaries (120347) 2004 SB60 and (42355) Typhon. *Icarus*, submitted.
- Stern, S.A., Buie, M.W., Trafton, L.M., 1997. HST high-resolution images and maps of Pluto. *Astron. J.* 113, 827, DOI: 10.1086/118304
- Sykes, M.V., 1999. IRAS survey-mode observations of Pluto–Charon. *Icarus* 142, 155–159.

- Trafton, L.M., Matson, D.L., Stansberry, J.A., 1998. Surface/atmosphere interactions and volatile transport: Triton, Pluto and Io. In “Solar System Ices”, Dordrecht Kluwer Academic Publishers, Astrophysics and Space Science Library Series 227. ISBN0792349024., p. 773.
- Verbiscer, A., French, R., Showalter, M., Helfenstein, P., 2007. Enceladus: cosmic graffiti artist caught in the act. *Science* 315, 815.
- Werner, M.W. et al., 2004. The Spitzer Space Telescope mission. *Astrophys. J. Sup. Ser.* 154, 1-9.
- Winnewisser, B.,K., Rao, N.N., Guelachvili, G., 1989. Infrared and Raman spectra of solid molecular nitrogen and hydrogen. In “Recent Trends in Raman Spectroscopy (S. B. Banerjee and S. S. Jha, Eds.)”, 143–159. World Scientific, Singapore.
- Wolters, S.D., Green, S.F., McBride, N., Davies, J.K., 2007. Thermal infrared and optical observations of four near-Earth asteroids. *Icarus* 193, 535–552.
- Young, E.F., Galdamez, K., Buie, M.W., Binzel, R.P., Tholen, D.J., 1999. Mapping the Variegated Surface of Pluto. *Astron. J.* 117, 1063–1076.
- Young, E.F., Binzel, R.P., Crane, K., 2001. A two-color map of Pluto’s sub-Charon hemisphere. *Astron. J.*, 121, 552–561.

Figure captions

Fig. 1. The entire set of MIPS observations of the Pluto-Charon system, consisting of 8 visits at the three MIPS wavelengths. Top two rows: 24 μm . Next two rows: 70 μm . Bottom two row: 160 μm . Note the asteroid contamination (665 Judith) on visit 2.

Fig. 2. Color-corrected 23.68 μm , 71.42 μm and 156 μm fluxes measured by *Spitzer-MIPS* over September 17-22, 2004. In this and other figures, fluxes were rescaled to an (arbitrary) distance to the observer of 30.95 AU. The mean heliocentric distance is 30.847 AU.

Fig. 3. IRS spectra. (Top): the eight IRS spectra over 21-37 μm , taken respectively at East longitudes of 33, 78, 122, 168, 213, 257, 302 and 348. Typical 1σ error bars of the brightness temperatures (T_B) are 0.3 K longwards of 26 μm . Superimposed are the eight MIPS 23.68 μm photometric points, taken at East longitudes of 37, 80, 127, 172, 218, 264, 307 and 351, and plotted without error bars. (Bottom): the IRS spectra are shown in the broader context of the MIPS 71.42 μm and 156 μm , and the earlier ISO data at 60, 100, 150, and 200 μm taken in 1997 (Lellouch et al. 2000). To account to first order for the change of heliocentric distance between 1997 (29.95 AU) and 2004 (30.84 AU), the ISO-derived T_B are rescaled by $\sqrt{29.95/30.84}$. At 60 and 100 μm where the lightcurve was clear, the ISO data are reinterpolated to the longitudes observed by MIPS. At 150 and 200 μm where ISO could not distinguish a lightcurve, the ISO data are simply averaged over

longitudes (“Mean ISO”). The ensemble of data clearly shows the trend for decreasing brightness temperatures with increasing wavelengths, though the situation longward of $100\ \mu\text{m}$ is unclear. The curves/points at different longitudes are distinguished by their colors. Note also that the longitude labels are ordered from the highest to the lowest brightness temperatures, and that some of the points (MIPS, ISO) are slightly offset in wavelength for clarity.

Fig. 4. The five 3-unit distributions of Pluto terrains used in this model, taken from Grundy and Fink (1996), Lellouch et al. (2000), and Grundy and Buie (2001).

Fig. 5. Pluto’s geometric albedo in 2002–2003 as a function of East longitude. Black dots: Observations (Buie et al. 2010a). The other five curves show best fit models with the five distributions of Fig. 4, using the equivalent geometric albedos in Table 3.

Fig. 6. Thermophysical model beaming factor ($\eta_{TPM}(\Theta)$) as a function of thermal parameter Θ and surface roughness, characterized by the mean slope angle ($\bar{\theta}$). “Smooth” ($\bar{\theta} = 10^\circ$), “Rough” ($\bar{\theta} = 33^\circ$) and “intermediate” ($\bar{\theta} = 20^\circ$) cases are shown. As expected, $\eta_{TPM}(\Theta)$ tends to 1 at large values of Θ , all the more than the surface is smoother.

Fig. 7. Fit of the MIPS data at 23.68 , 71.42 and $156\ \mu\text{m}$ using the Lellouch et al. (2000) distribution (g_2) of terrains. Black points with error bars: observations. Blue: best fit model. This model uses the spectral emissivities

of Fig. 8. The bolometric emissivity of methane $\epsilon_b(\text{CH}_4)$ is equal to 0.7. The thermal parameter is $\Theta_{Ch} = 4.5$ for Charon and $\Theta_{Pl} = 6$ for Pluto. This model allows an almost perfect match at $23.68 \mu\text{m}$. At $71.42 \mu\text{m}$, it provides a satisfactory compromise between the MIPS data and the ISO measurements rescaled – in an approximate fashion – to the same heliocentric distance (red points), while at $156 \mu\text{m}$, it somewhat overpredicts the observed T_{BS} . The green curve is an alternate model, with $\epsilon_b(\text{CH}_4) = 0.855$, $\Theta_{Ch} = 3.5$, $\Theta_{Pl} = 6$. In this case, the spectral emissivities of CH_4 and tholin/ H_2O do not follow Fig. 5, but are instead equal to 0.7 at $70 \mu\text{m}$ and 0.5 at $160 \mu\text{m}$. This alternate model allows an overall improved fit of the MIPS 71.42 and $156 \mu\text{m}$ T_{BS} , but the associated spectral behaviour is unexpected (see text). In the top panel, the red curve shows the effect of using a CH_4 $24 \mu\text{m}$ spectral emissivity of 0.35, leading to a strong lack of flux at $L = 250\text{--}50$.

Fig. 8. Spectral emissivities of the three units for the best fit of Fig. 7 and 9.

Fig. 9. Overall fit of the IRS, MIPS and ISO data with the best fit model using the Lellouch et al. (2000) distribution (g_2) of terrains and the spectral emissivities of Fig. 8. A satisfactory match of the IRS spectra is achieved, as well as a good compromise between all data up to $\sim 100 \mu\text{m}$. The same color codes as in Fig. 3 are used.

Fig. 10. Fit of the ISO $60\text{-}\mu\text{m}$ (top) and $100\text{-}\mu\text{m}$ (bottom) lightcurves, using the g_2 distribution of terrains. The same model as in Fig. 9 is used,

but is here run for the geometric conditions of the ISO observations ($R_h = 29.95$ AU and a subsolar latitude $\beta = 19^\circ$).

Fig. 11. Fit of the MIPS 24- μm lightcurve with the five distributions of terrains and the two values for the bolometric emissivity of methane (0.855 and 0.70) considered in this paper. Solutions in terms of the thermal parameters of Pluto and Charon are given (see also Table 4). Distributions g_3 and b_1 provide worse fits than the other three distributions. The bottom panel shows the effect of using a CH_4 24 μm spectral emissivity of 0.35.

Fig. 12. Contribution of the various units to the MIPS 24- and 70- μm lightcurves for the g_2 and b_3 distributions. The contribution of N_2 ice is negligible at 24 μm .

Fig. 13. Comparison of the *Spitzer-MIPS* observations of April 2007 (blue stars) and September 2004 (black dots), at 24 μm (top) and 70 μm (bottom). Solid black line: nominal model for 2004 (also shown as the blue line in Fig. 7). Blue line: same model, applied to the April 2007 geometry (heliocentric distance, subsolar latitude). Despite the increased heliocentric distance (31.27 AU vs 30.85 AU), the model cannot account for the decrease of the brightness temperatures of Pluto-Charon over 2004-2007 (by ~ 0.5 K at 24 μm and ~ 2 K at 70 μm). The slightly lower amplitude of the model lightcurves for 2007 is related to the increase of the subsolar latitude (39° vs 34.5°), which is also responsible for a slight increase in Charon's contribution.

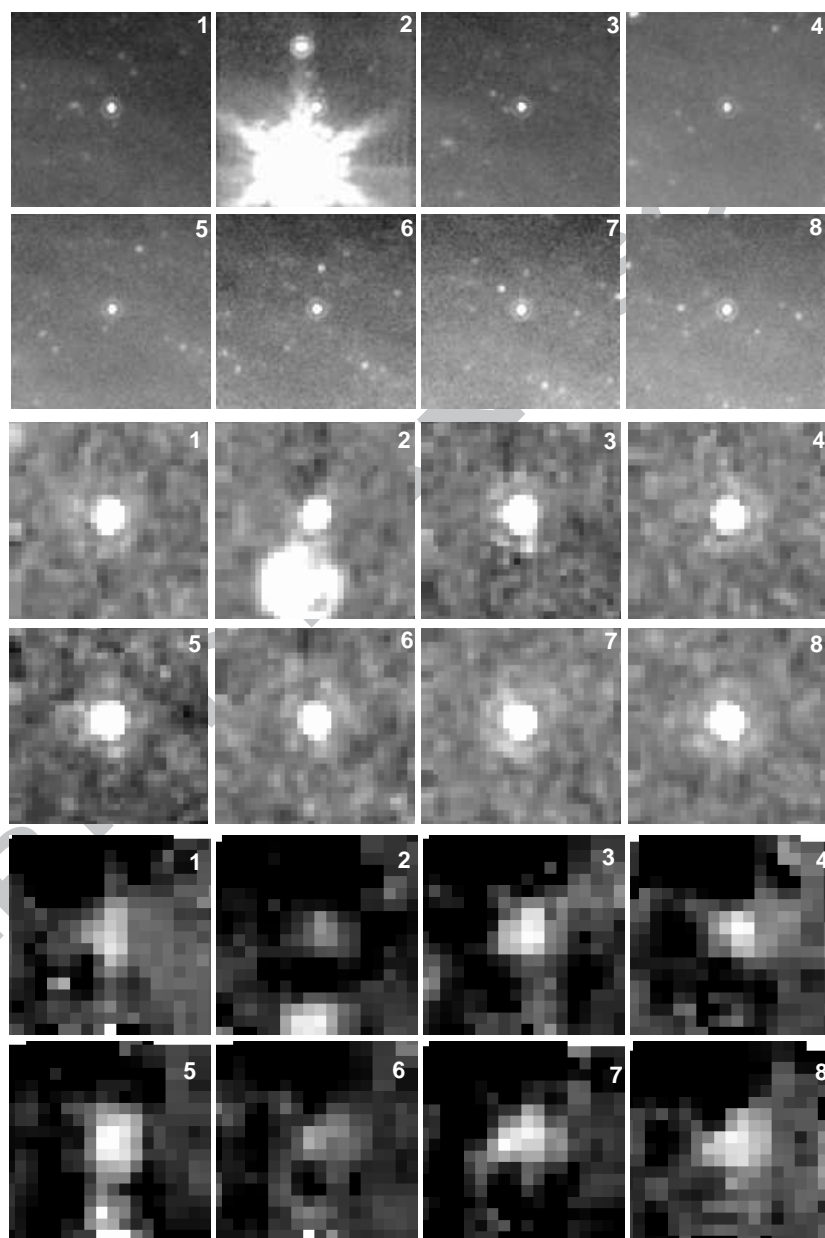


Fig. 1

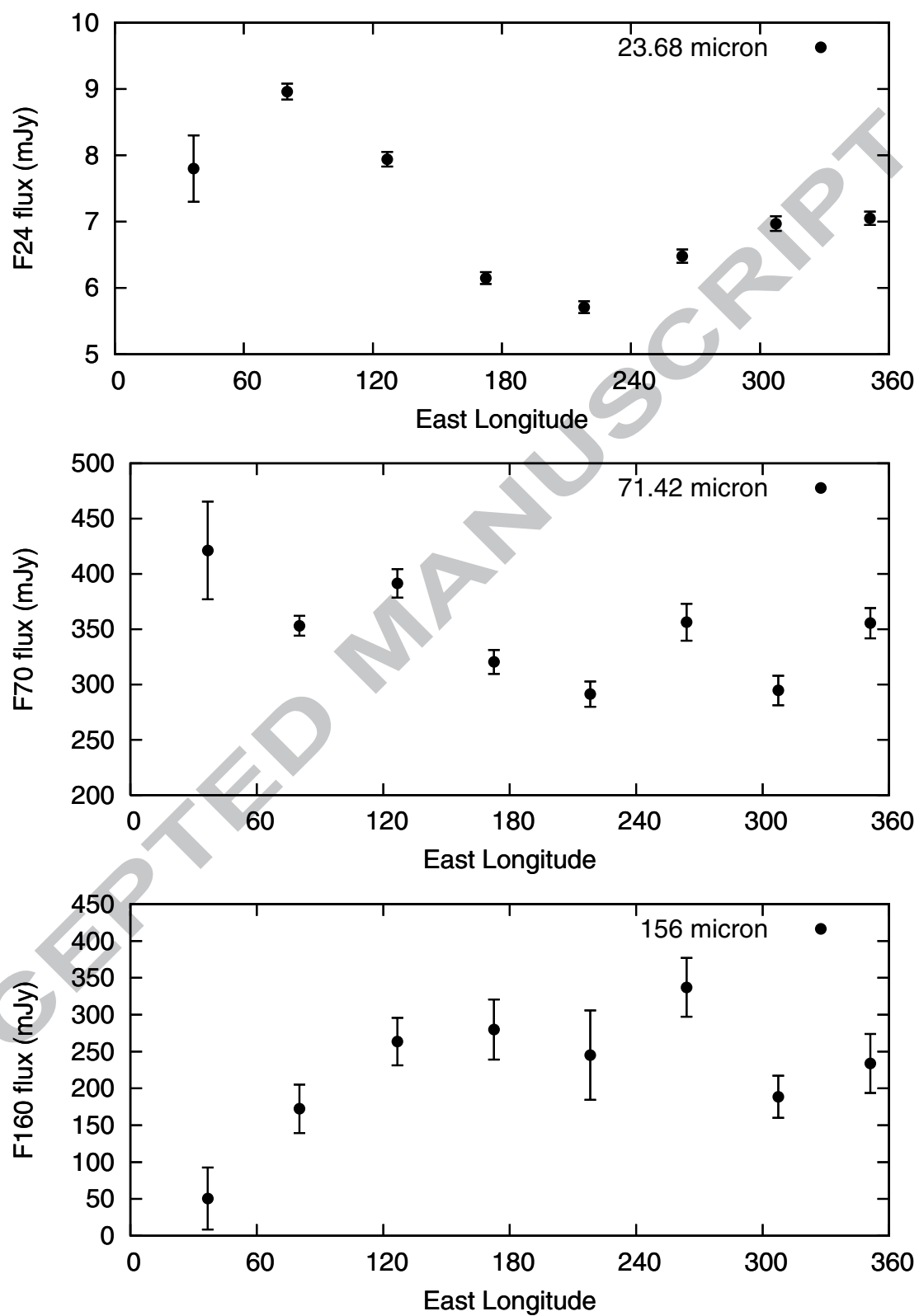


Fig. 2

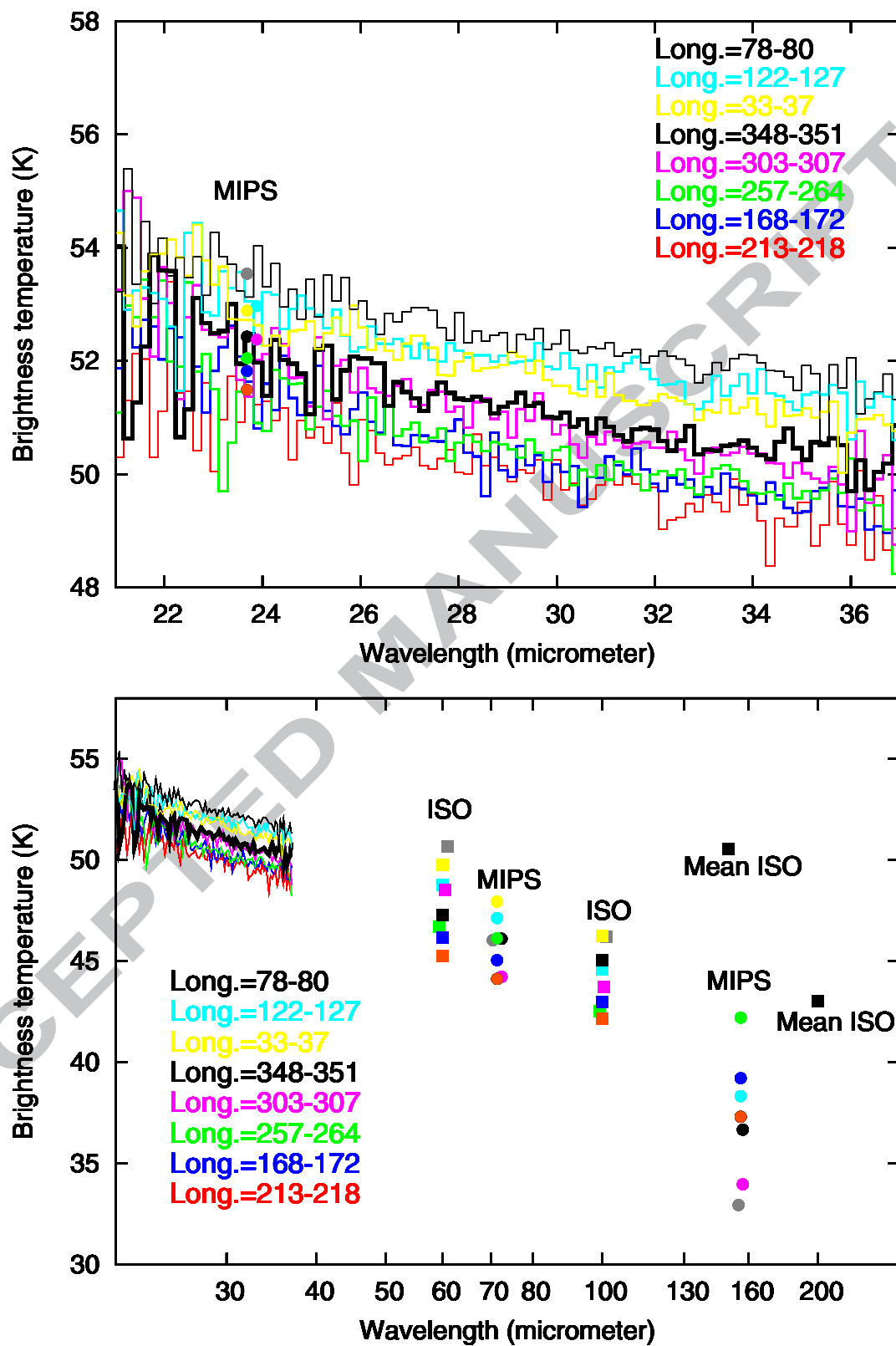


Fig. 3

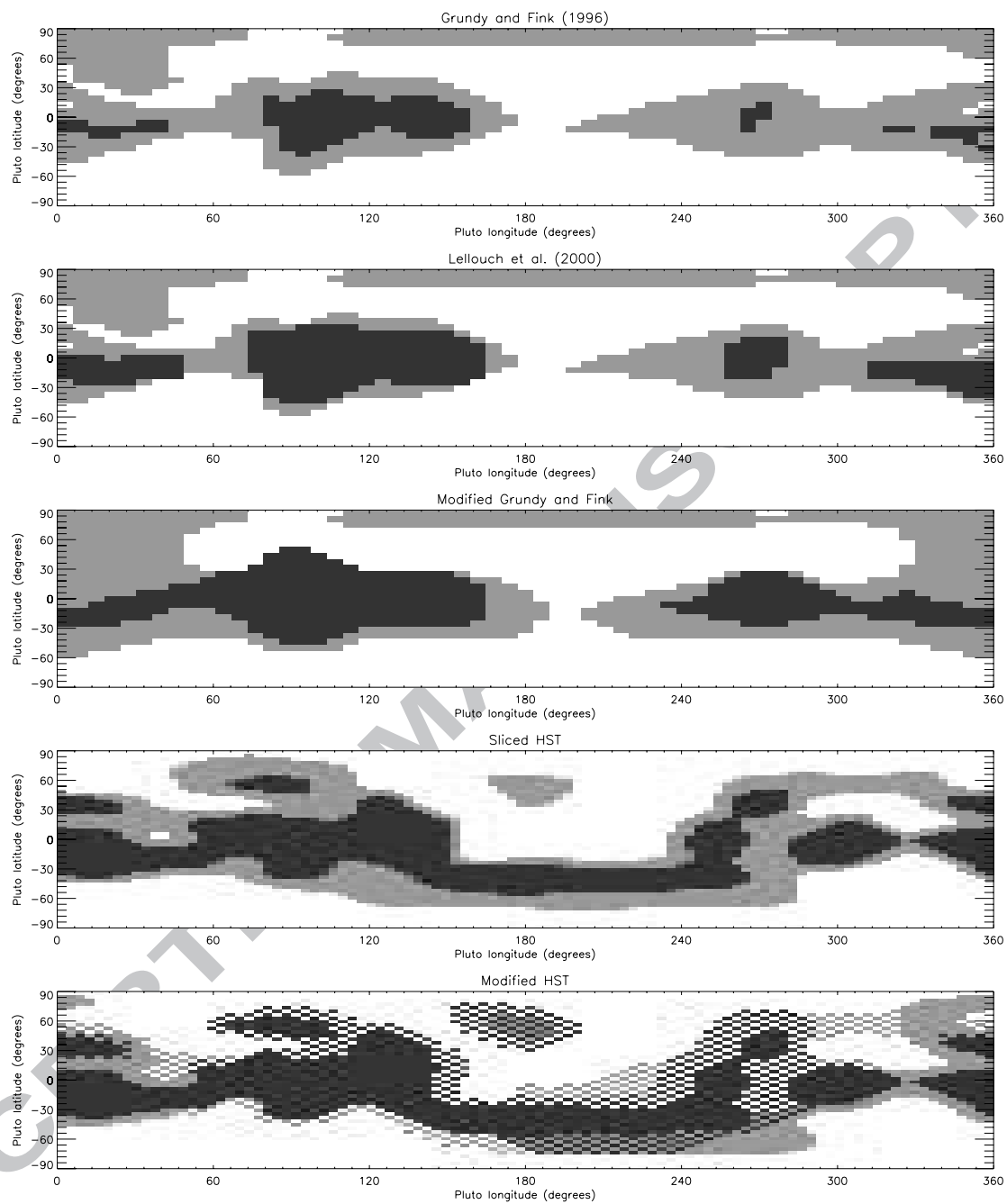


Fig. 4

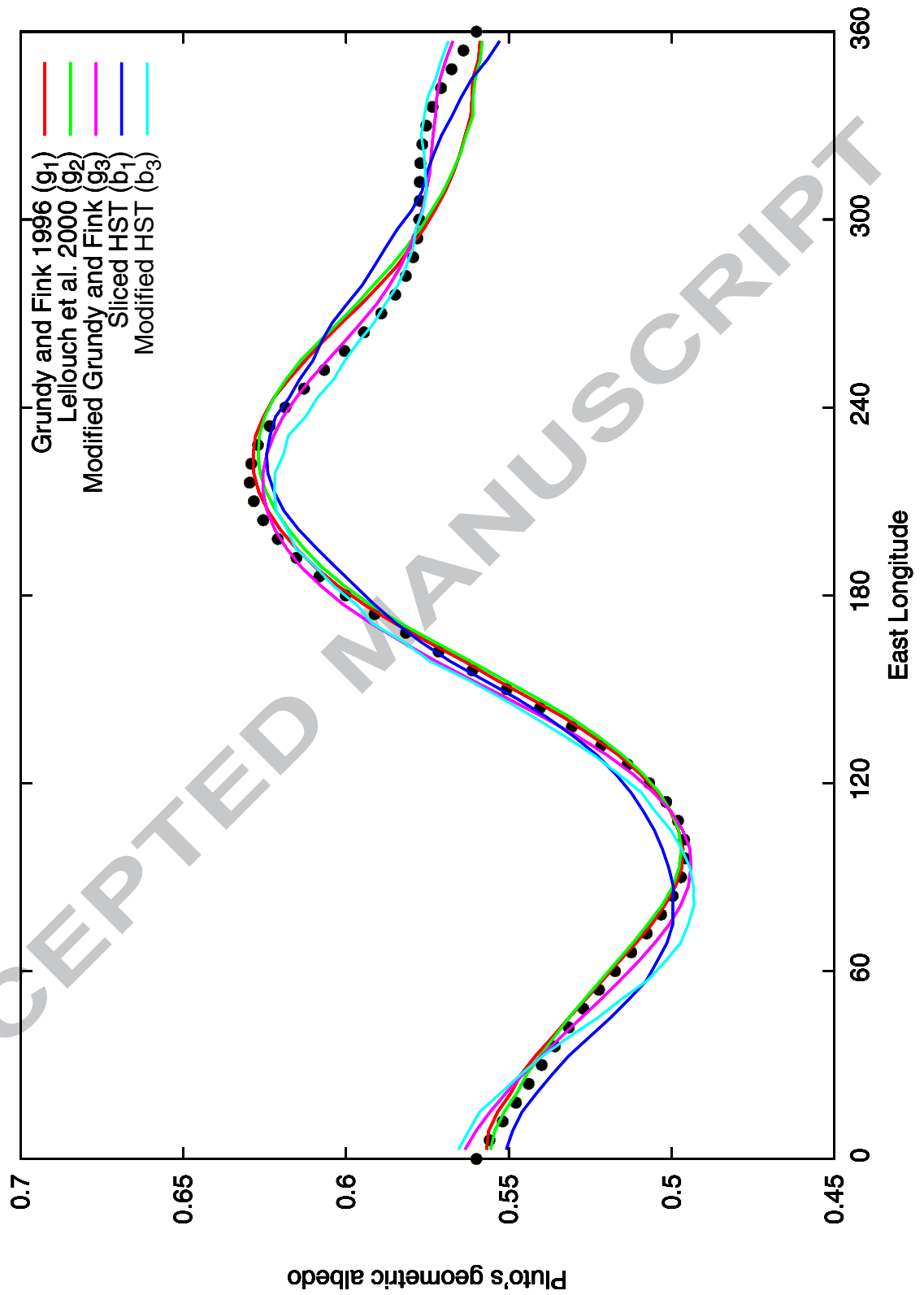


Fig. 5

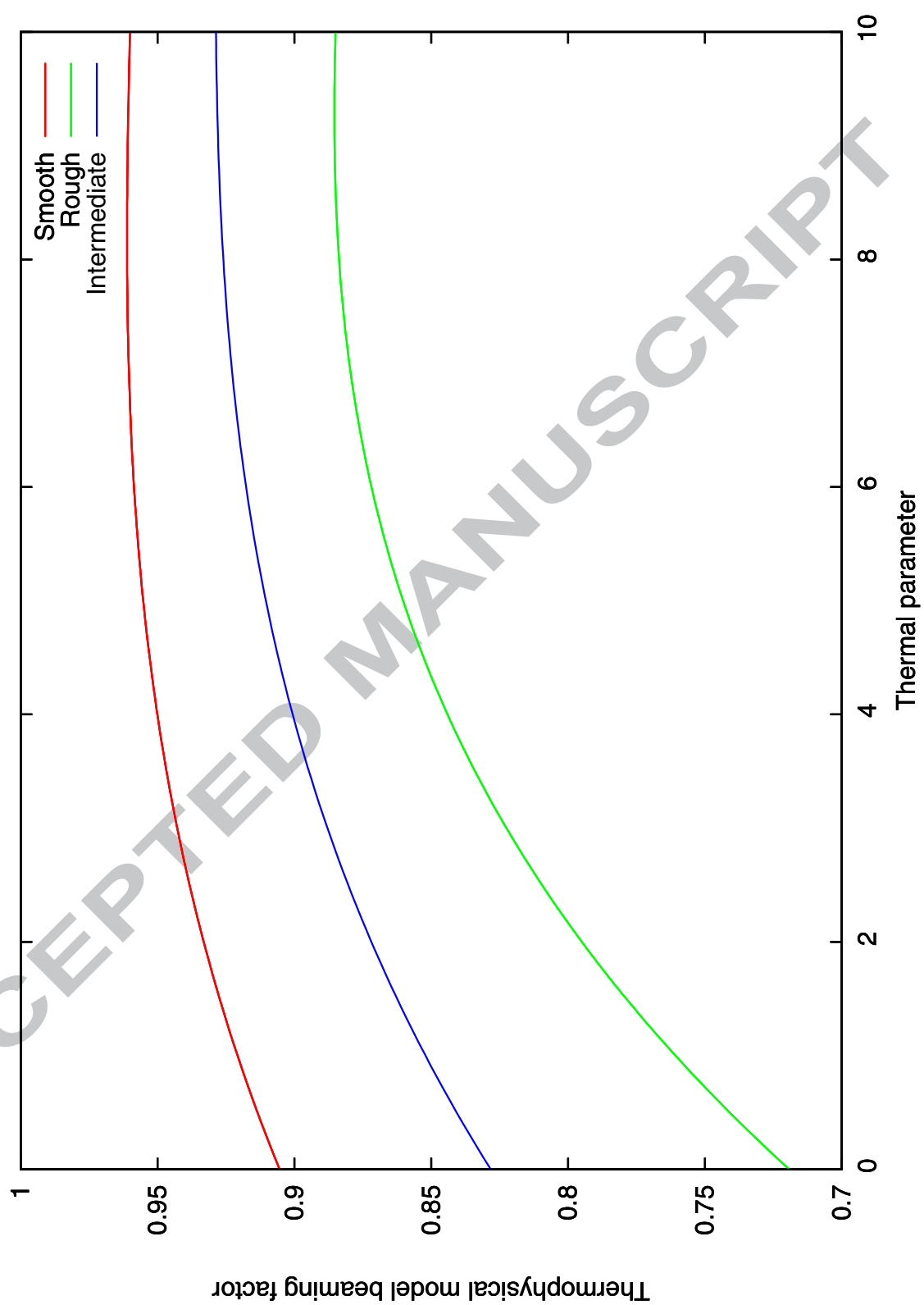


Fig. 6

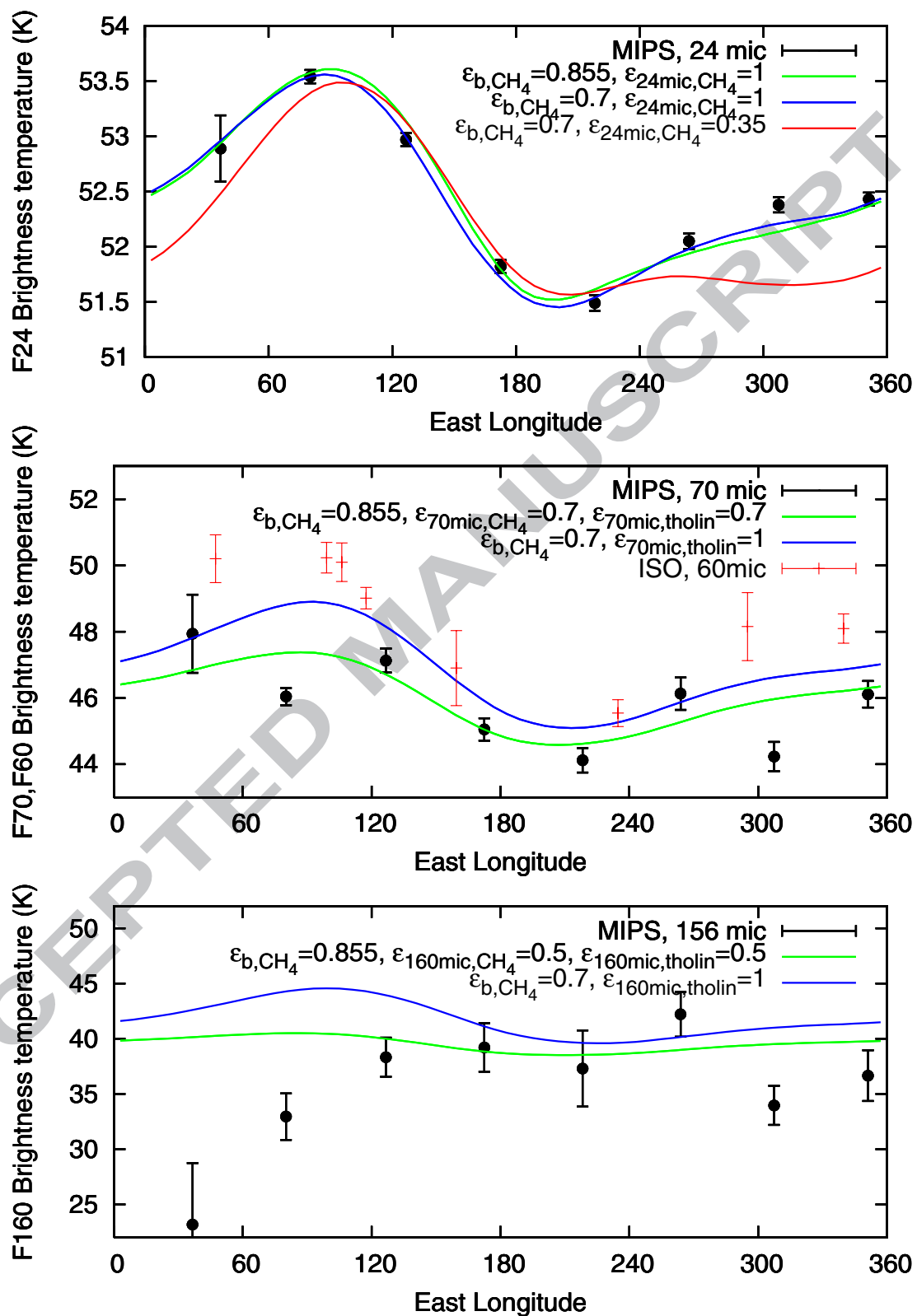


Fig. 7

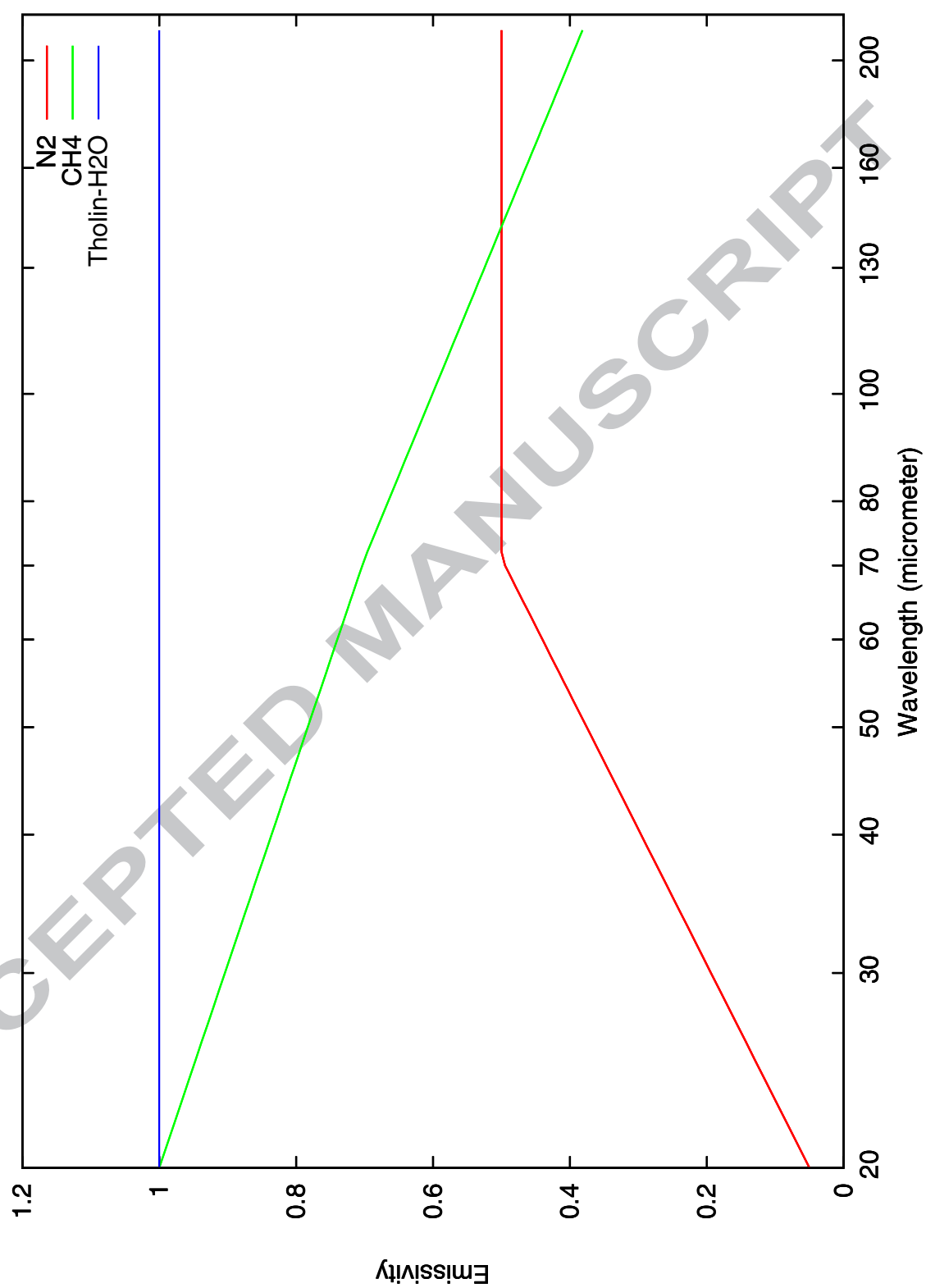


Fig. 8

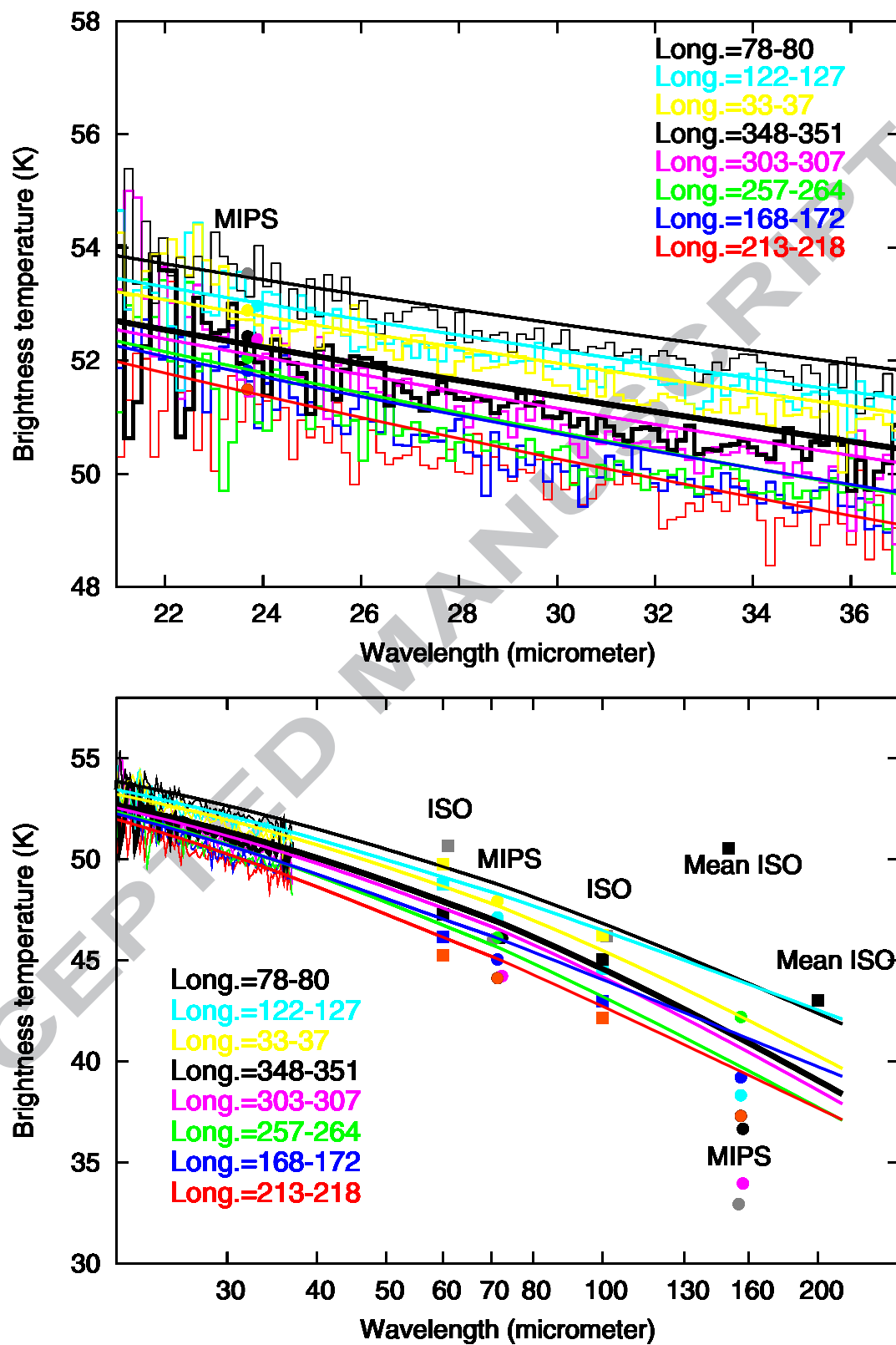


Fig. 9

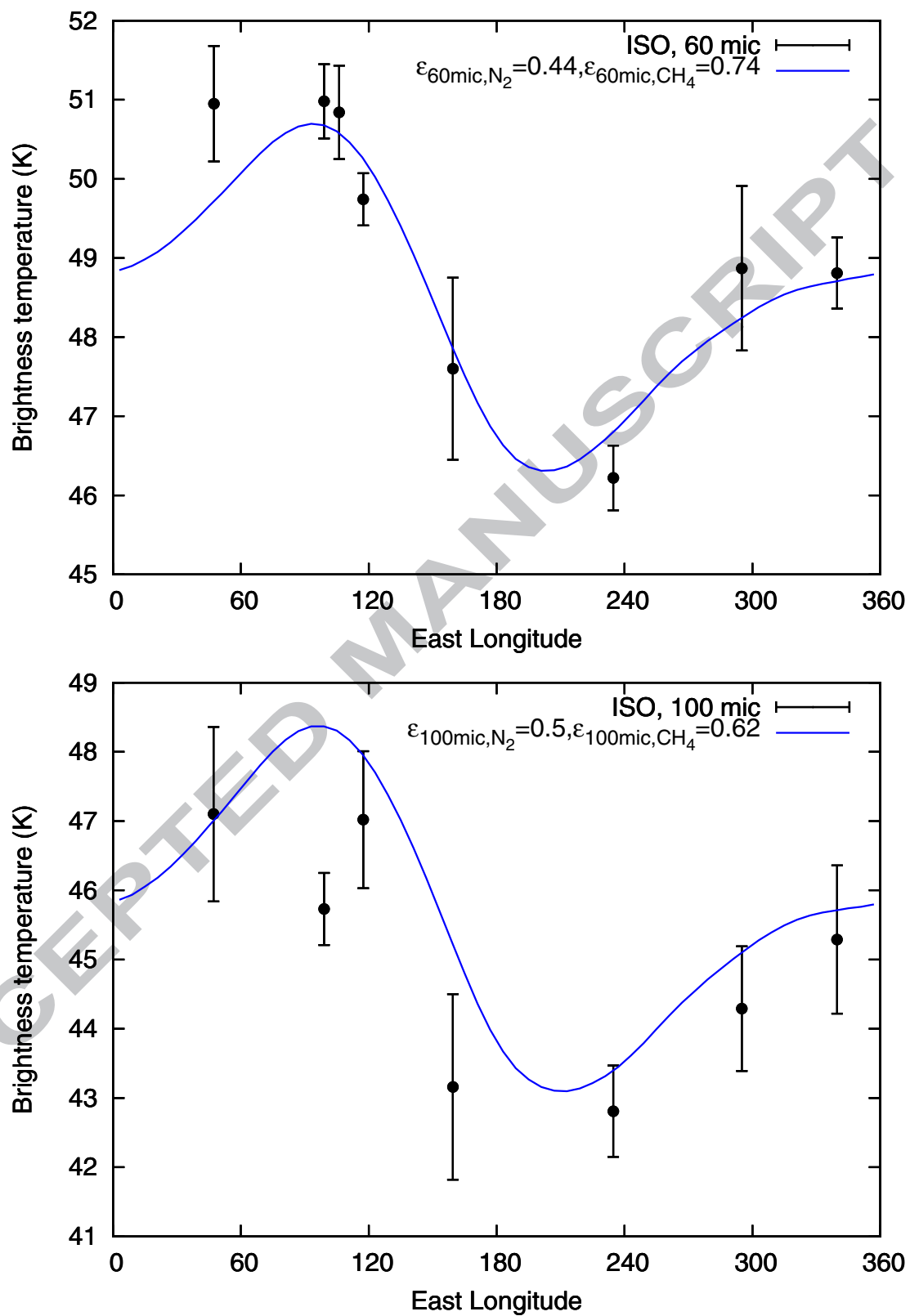


Fig. 10

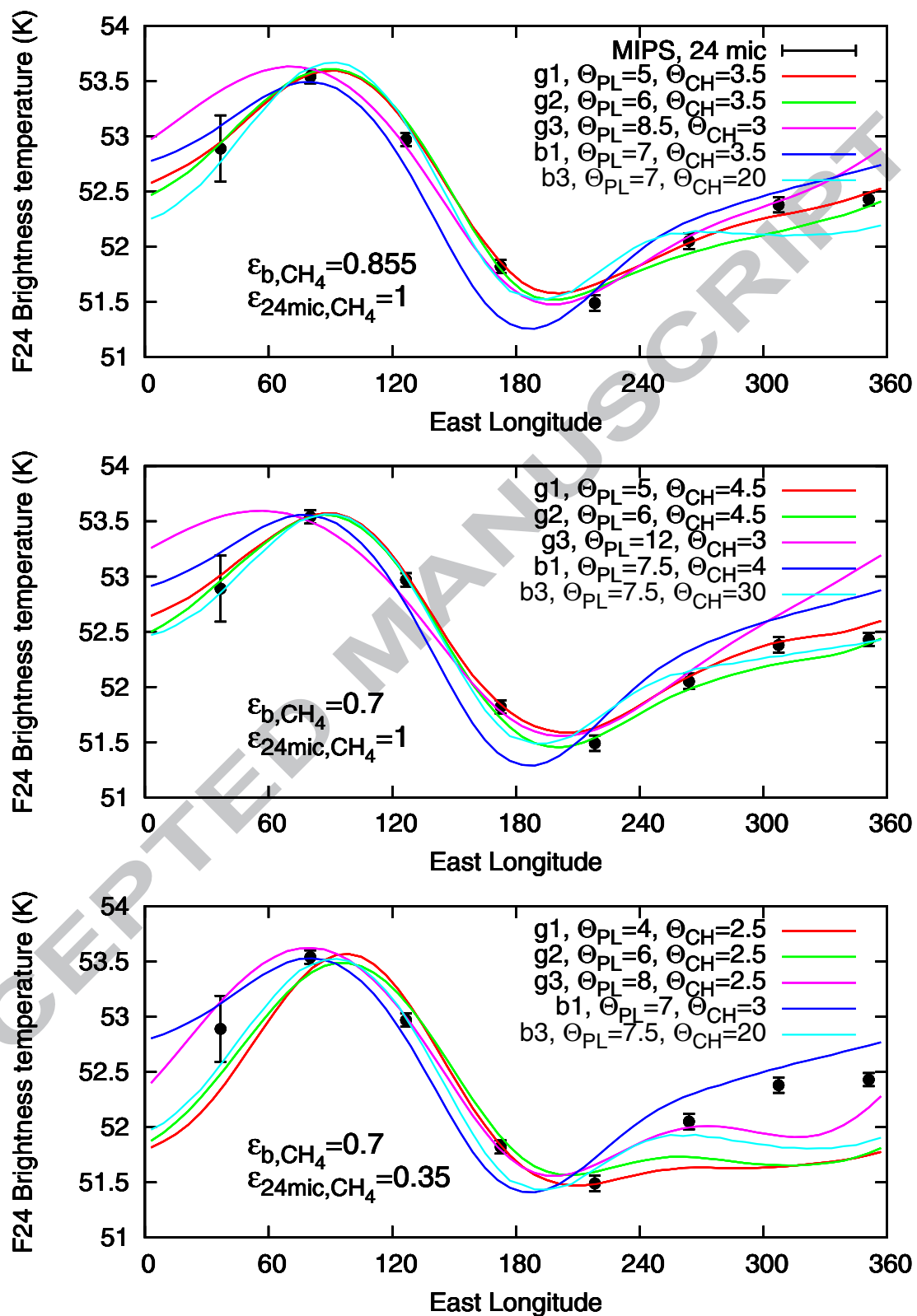


Fig. 11

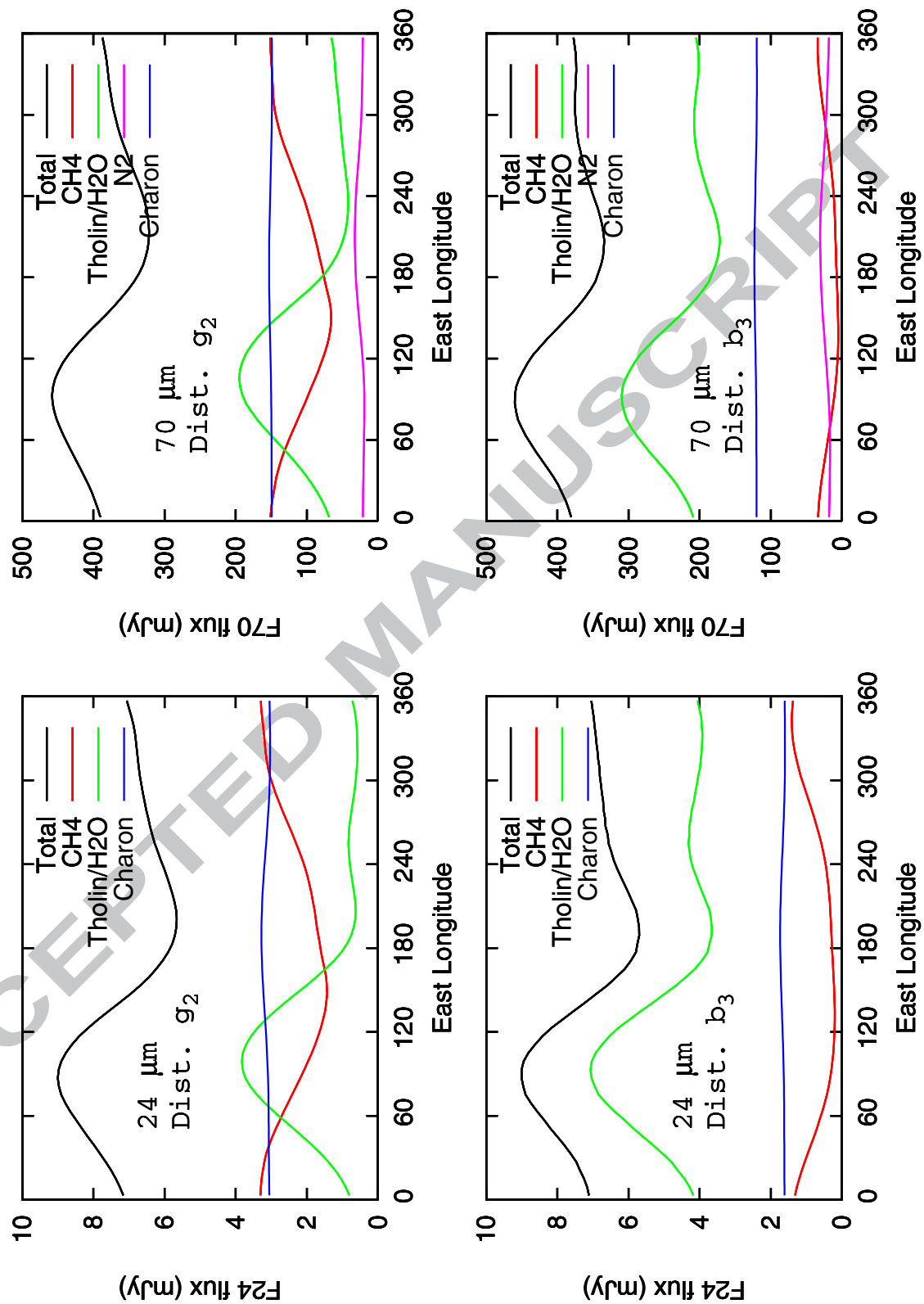


Fig. 12

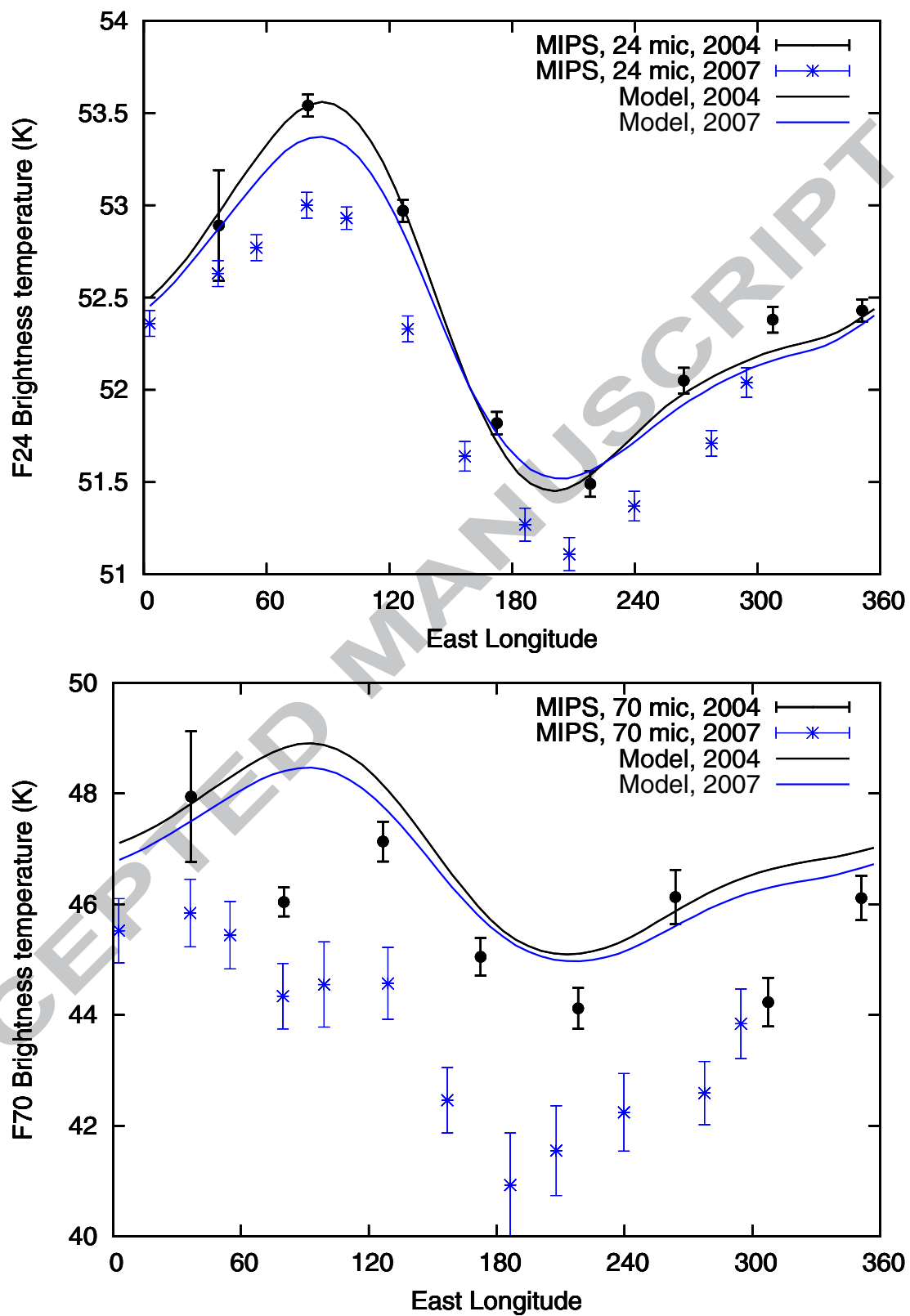


Fig. 13

Table 1: Observational circumstances and fluxes for the Spitzer/MIPS spectra

Date (UT)	Start Time (UT)	Longitude ^a	R _h (AU)	Δ (AU)	F24 (mJy)	F 70 (mJy)	F160 (mJy)
2004-09-17	04:42	80.2	30.8463	30.832	9.03±0.12	355.8±8.99	173.6±33.1
2004-09-17	23:13	36.7	30.8468	30.835	7.85±0.50	424.1±44.47	50.9±42.4
2004-09-18	18:32	351.1	30.8470	30.859	7.09±0.10	357.6±13.79	235.3±40.2
2004-09-19	13:37	307.4	30.8474	30.873	7.00±0.11	296.1±13.43	189.5±28.6
2004-09-20	07:57	263.9	30.8477	30.886	6.51±0.10	357.8±16.80	338.5±40.1
2004-09-21	03:08	218.2	30.8480	30.899	5.73±0.09	292.2±11.45	246.0± 60.8
2004-09-21	22:41	172.5	30.8483	30.913	6.16±0.09	321.2±10.90	280.6±40.8
2004-09-22	18:12	126.7	30.8487	30.927	7.95±0.11	392.0±12.90	263.9±32.2

^a Sub-observer East longitude at mid-point. We adopt the same orbital conventions as e.g. in Buie et al. (1997) and Lellouch et al. (2000)

Table 2: Observational circumstances for the *Spitzer*/IRS spectra

Date (UT)	Start Time (UT)	Longitude ^a	R _h (AU)	Δ (AU)
2004-08-27	11:26	168	30.8376	30.487
2004-08-28	07:24	122	30.8379	30.500
2004-08-29	02:02	78	30.8383	30.513
2004-08-29	20:58	33	30.8386	30.525
2004-08-30	16:17	348	30.8389	30.539
2004-08-31	11:33	303	30.8393	30.552
2004-09-01	07:01	257	30.8396	30.565
2004-09-02	01:49	213	30.8399	30.578

^a Sub-observer East longitude at mid-point. We adopt the same orbital conventions as e.g. in Buie et al. (1997) and Lellouch et al. (2000)

Table 3. Adopted geometric albedo of the various units

Unit	Geographical terrain model				
	g ₁ : Grundy and Fink (1996)	g ₂ : Lellouch et al. (2000)	g ₃ : Modified Grundy and Fink ¹	b ₁ Sliced HST ¹	b ₃ Modified HST ¹
N ₂	0.74	0.73	0.71	0.69	0.83
CH ₄	0.46	0.51	0.62	0.80	0.73
Tholin/H ₂ O	0.17	0.25	0.30	0.16	0.22
Charon	0.392-0.428 ²				

¹ Grundy and Buie (2001)² Valid for all five distributions

Table 4. Best fit parameters for the five distributions

Distrib.	Input parameters			Fitted parameters				Comment
	Tholin ϵ_b	CH ₄ ϵ_b $\epsilon_{24\mu m}$		Θ_{Pl}	Θ_{Ch}	CH ₄ $\epsilon_{70\mu m}$	Tholin $\epsilon_{70\mu m}$	
g ₁	1	0.85	1	5	3.5	0.7	0.7	Inconsistencies in ϵ_{CH_4} and ϵ_{tholin}
	1	0.70	1	5	4.5	0.75	1	Good fit
	1	0.70	0.35	4	2.5	0.5	1	Poor 24 μm fit
g ₂	1	0.85	1	6	3.5	0.7	0.7	Inconsistencies in ϵ_{CH_4} and ϵ_{tholin}
	1	0.70	1	6	4.5	0.7	1	Good fit
	1	0.70	0.35	6	2.5	0.5	1	Poor 24 μm fit
g ₃	1	0.85	1	8.5	3	0.7	0.7	Poor 24 μm fit + inconsistencies
	1	0.70	1	12	3	0.5	1	Poor 24 μm fit
	1	0.70	0.35	8	2.5	0.5	1	Acceptable fit
b ₁	1	0.85	1	7	3.5	0.7	0.7	Poor 24 μm fit + inconsistencies
	1	0.70	1	7.5	4	0.5	1	Poor fit
	1	0.70	0.35	7	3	0.5	1	Poor fit
b ₃	1	0.85	1	7	20	0.75	0.75	Inconsistencies in ϵ_{CH_4} and ϵ_{tholin}
	1	0.70	1	7.5	30	0.3	1	Good fit but inconsistency in ϵ_{CH_4}
	1	0.70	0.35	4	2.5	0.3	1	Poor 24 μm fit, inconsistency in ϵ_{CH_4}

- Thermal lightcurve observations of the Pluto-Charon system with Spitzer
- Multi-terrain thermophysical model.
- Determination of the thermal properties of Pluto and Charon
- Emissivity properties of Pluto's surface